This is a preprint, the final version is subject to change, of the American Mineralogist (MSA)
Cite as Authors (Year) Title. American Mineralogist, in press.
DOI: https://doi.org/10.2138/am-2020-7359

Revision 1

Quantitative microscale Fe redox imaging by multiple energy X-ray fluorescence mapping at the Fe K pre-edge peak

Eric T. Ellison[a]*, Lisa E. Mayhew[a], Hannah M. Miller[a], and Alexis S. Templeton[a]

[a]Department of Geological Sciences, UCB 399, University of Colorado – Boulder, Boulder, CO 80309, USA

*Corresponding author

Keywords: Iron, redox, oxidation state, X-ray fluorescence mapping, microscale, pre-edge, serpentinization, Oman ophiolite

This is a preprint, the final version is subject to change, of the American Mineralogist (MSA)
Cite as Authors (Year) Title. American Mineralogist, in press.
DOI: https://doi.org/10.2138/am-2020-7359

Abstract

Fe oxidation/reduction reactions play a fundamental role in a wide variety of geological processes. In natural materials, Fe redox state commonly varies across small spatial scales at reaction interfaces, yet the approaches available for quantitatively mapping the Fe redox state at the microscale are limited. We have designed an optimized synchrotron-based X-ray spectroscopic approach that allows microscale quantitative mapping of Fe valence state by extending the Fe XANES pre-edge technique. An area of interest is mapped at 9 energies between 7109 eV-7118 eV and at 7200 eV, allowing reconstruction, baseline subtraction, and integration of the pre-edge feature to determine Fe(III)/∑Fe with 2 μm spatial resolution. By combining the Fe redox mapping approach with hyperspectral Raman mineralogy mapping, the Fe oxidation state distributions of the major mineral phases are revealed. In this work, the method is applied to a partially serpentinized peridotite with a variety of Fe-bearing secondary mineral phases in order to trace the Fe transformations and redox changes that occurred during its alteration. Analysis with the Fe redox mapping technique revealed that the peridotite contained relict olivine with abundant Fe(II), while serpentine, pyroaurite, and another hydroxide phase are secondary mineral reservoirs of Fe(III). Although serpentine is not Fe-rich, it contained approximately 74% ± 14% Fe(III)/∑Fe. These analytical results are integral to interpreting the sequence of alteration reactions; serpentinization of primary olivine formed Fe(II)-rich brucite and oxidized serpentine, which could have contributed to H_2 production during serpentinization. Subsequent weathering by oxidizing, CO_2-bearing fluids led to the partial carbonation and oxidation of brucite, forming pyroaurite and a hydroxide phase containing dominantly Fe(III). This Fe redox imaging approach is applicable to standard petrographic thin sections or grain mounts and can be applied to a variety of geologic and biogeochemical systems.

This is a preprint, the final version is subject to change, of the American Mineralogist (MSA)
Cite as Authors (Year) Title. American Mineralogist, in press.
DOI: https://doi.org/10.2138/am-2020-7359

Introduction

Fe oxidation and reduction reactions during mineral dissolution and precipitation play a dominant role in numerous geological and environmental processes; thus, determining the Fe redox state (Fe(III)/∑Fe) of natural materials has many applications. For example, Fe redox reactions exert a fundamental control on chemical weathering in mine drainage systems (Johnson et al. 2014), bedrock weathering and saprolitization (Buss et al. 2008), soil nutrient cycling and availability (Prietzel et al. 2007; Colombo et al. 2014), iron transport and bioavailability in the oceans (Lam et al. 2012; Toner et al. 2012), and stabilization or mobilization of groundwater contaminants including uranium, selenium, and arsenic (Myneni et al. 1997; O'Loughlin et al. 2003; Essilfie-Dughan et al. 2013; Ying et al. 2013). Additionally, iron valence can help constrain the oxygen fugacity of geological materials, revealing key insights into mantle processes and planetary formation (Berry et al. 2008; Cottrell and Kelley 2011; Elmaleh et al. 2015; Le Guillou et al. 2015).

There is a need for spatially-resolved methods to determine Fe redox in complex systems at the microscale. The progression of Fe redox reactions in many systems may be recorded by gradients in Fe(II)/(III) over small spatial scales. The spatial scale may be set by the grain- and pore-size, or by localization of the water-particle or microbe-particle interface involved in the redox reaction. Mossbauer spectroscopy and wet chemical titration methods for quantifying Fe valence state give excellent results at the bulk scale, but other methods are required at the microscale.

X-ray absorption near edge spectroscopy (XANES) is often used to probe the average iron oxidation state, both at the bulk scale and through micro-scale spot analyses. This approach can be applied either with soft X-rays at the Fe $L_{2,3}$ edges (Toner et al. 2009) or with hard X-rays

This is a preprint, the final version is subject to change, of the American Mineralogist (MSA)
Cite as Authors (Year) Title. American Mineralogist, in press.
DOI: https://doi.org/10.2138/am-2020-7359

61 at the Fe K edge (Bajt et al. 1994; Marcus et al. 2008; Farges and Wilke 2016). The shape and
62 structure of the K-edge absorption spectrum contains information on both the valence and
63 coordination environment of Fe, which can confound efforts to extract an estimate of the Fe
64 redox state (Brown et al. 1988).

65 Existing methods, detailed below, allow qualitative mapping of the average Fe oxidation
66 state at the microscale, and quantitative mapping is possible for single minerals (e.g. garnet) and
67 glasses. Other methods exist at the nanoscale or with intensive sample preparation. However, no
68 existing method allows quantitative mapping on a standard petrographic thin section with
69 complex mineralogy.

70 Application of XANES-based techniques to image average Fe oxidation state at the
71 microscale has been a long-term challenge. One approach is to collect microscale X-ray
72 Fluorescence (XRF) maps at several energies across the main absorption edge and use linear
73 fitting of spectra from end-member standards to generate qualitative distribution maps of Fe(II)
74 and Fe(III) (e.g. Templeton et al. 2009; Lam et al. 2012). The shape of the K-edge of Fe varies
75 strongly between different crystalline Fe-bearing compounds, even of the same valence, because
76 it is sensitive to the coordination, site geometry, and bonding with nearest and more distant
77 neighbors (Brown et al. 1988). Therefore, methods based on least-squares fitting to two (or
78 more) Fe-valence standards are limited in accuracy by the spectroscopic similarity between the
79 material being analyzed and the standards (Marcus 2010). In complex geological thin sections
80 with many mineral species, some of which may be difficult to obtain standards for, this becomes
81 problematic. Results derived from this method are therefore generally considered qualitative
82 only. The approach of XRF mapping at multiple energies along the Fe K-edge has been extended
83 using principal components analysis to identify spectroscopic endmembers within the sample as

84 candidate components for linear fitting in order to identify and qualitatively image distinct Fe
85 species (Mayhew et al. 2011). Garnet-specific calibrations of Fe redox have allowed quantitative
86 Fe redox mapping based on multiple energy mapping of garnet with very high precision (Berry
87 et al. 2010, 2013) as well as spatially resolved microscale transects (Mino et al. 2014).
88 Multivariate statistical models have recently been used to select several energies for quantitative
89 Fe redox mapping in lunar glasses (McCanta et al. 2019). Finally, the development of
90 synchrotron beamlines with dispersive optics have allowed fast hyperspectral XRF imaging, and
91 this approach has been used to qualitatively map Fe redox (Muñoz et al. 2006; Andreani et al.
92 2013), and to quantitatively map the average redox state of elements other than Fe (e.g. As,
93 Etschmann et al. 2010).

94 Most quantitative work has focused on the pre-edge peak (~7108 eV to 7118 eV), an
95 absorption feature located at energies just below the main Fe K-edge. While features of the main
96 edge region (7120 eV to 7200 eV) are also sensitive to valence state, these features are more
97 strongly dependent on the specific atomic environment of Fe, and thus are more strongly
98 influenced by the crystal structure, chemical composition, and Fe coordination of the material
99 (Brown et al. 1988). The position of the pre-edge peak is sensitive to Fe valence in a relatively
100 predictable way (Calas and Petiau 1983; Waychunas et al. 1983), and was used to quantify
101 Fe(III)/∑Fe by Bajt et al. (1994) and subsequently by many others. Wilke et al. (2001) developed
102 a method to estimate the average Fe redox of Fe(II) and Fe(III)-bearing mineral mixtures while
103 accounting for the confounding effect of different Fe coordination environments, using a plot of
104 integrated intensity vs. the centroid energy position of the pre-edge peak, called a "variogram".
105 Orientation effects on the observed pre-edge peak structure represent an added challenge to
106 performing these analyses at the microscale, however much work has been done to perfect the

This is a preprint, the final version is subject to change, of the American Mineralogist (MSA)
Cite as Authors (Year) Title. American Mineralogist, in press.
DOI: https://doi.org/10.2138/am-2020-7359

calibration of XANES methods and increase the accuracy of these Fe(III)/∑Fe determinations (Dyar et al. 2002a; Marcus et al. 2008; Dyar et al. 2012; Muñoz et al. 2013; Dyar et al. 2016b). Still, the Fe pre-edge technique has not been applied quantitatively to 2D mapping of the average Fe redox in crystalline minerals at the microscale.

Here we describe a method for the collection of quantitative Fe redox maps with microscale resolution on standard petrographic thin sections by collecting multiple energy μXRF maps along the Fe pre-edge peak. We apply this method to a partially altered serpentinite rock from the Samail Ophiolite (located in the Sultanate of Oman) with relict primary mineral phases and hydrated alteration features that optically exhibited a sharp redox gradient. Using a configuration common to many micro-focused hard X-ray beamlines (fluorescence detection and a mapping stage), we are able to image ~200,000 μm^2 in approximately 11 hours with a spatial resolution of 2 x 2.8 μm. This resolution allowed us to observe significant Fe(III) in fine-textured and intermixed secondary minerals surrounding olivine. We combine this redox map with co-registered hyperspectral Raman mineralogy maps at similar spatial resolutions to estimate the overall Fe(III)/∑Fe of the different mineral phases, although the analysis depth of the techniques differ, likely leading to imperfect co-registration. This approach to mapping average Fe redox allowed us to assess the important reservoirs of Fe(II) and Fe(III) in this complex mineral assemblage and infer the sequence of alteration reactions that led to its formation.

This is a preprint, the final version is subject to change, of the American Mineralogist (MSA)
Cite as Authors (Year) Title. American Mineralogist, in press.
DOI: https://doi.org/10.2138/am-2020-7359

125 # Methods

126 ## Sample OM14-07

127 We studied a partially serpentinized peridotite rock collected from a surface outcrop at
128 Wadi Lufti in the Oman ophiolite (described in Mayhew et al. 2018), which we selected for its
129 striking apparent Fe redox contrasts. The weathered surface rinds were cut away with a diamond
130 saw and a ~30 μm thick polished thin section was prepared for analysis. The sample was
131 examined in plane-polarized transmitted light to select the area of interest and make an initial
132 assessment of the apparent Fe-bearing phases and their likely redox state (based on mineral
133 identification or color). To facilitate the precise alignment of maps collected with different
134 microscale analytical techniques, a diamond scribe was used to etch fiducial marks into the
135 sample surface. These marks were then filled with TiO_2 powder by spreading a suspension of
136 TiO_2 in ethanol over the sample, allowing it to dry, and then wiping away the excess TiO_2. TiO_2
137 was chosen because the Ti X-ray fluorescence can be detected when excited by X-rays at the Fe
138 K-edge and because the crystal polymorphs anatase and rutile both produce intense, easy to
139 detect Raman peaks. TiO_2 fiducial marks can therefore be detected in both Raman and XRF
140 maps, without interfering with those analyses since Ti-bearing minerals are not abundant in
141 serpentinized peridotite rocks. The sample was subsequently re-polished, cleaned, and carbon-
142 coated prior to EMPA analyses, and this resulted in the removal of the TiO2 from the fiducial
143 marks.
144
145 ## Electron Probe Microanalysis

146 Quantitative electron probe microanalysis (EPMA) maps were collected on a JEOL JXA-
147 8230 by stage mapping with a 1 μm beam size and step size, 15kV accelerating voltage, 20 nA

This is a preprint, the final version is subject to change, of the American Mineralogist (MSA)
Cite as Authors (Year) Title. American Mineralogist, in press.
DOI: https://doi.org/10.2138/am-2020-7359

current, and 120 ms dwell time. Map collection was performed with ProbeImage software (Probe Software Inc.), and quantifications were determined using ZAF matrix correction (Armstrong/Love Scott algorithm) and mean atomic number background correction in CalcImage software (Probe Software Inc.). Representative analyses of specific mineral phases were extracted from the quantitative maps by averaging over regions of the map containing each phase.

Raman spectroscopy

Raman spectroscopy is a fast, non-destructive technique that can provide insight into the molecular and crystal structures of materials also at the microscale. The responsiveness of the Raman spectra to crystal structure allows for phase identification as well as the discrimination of polymorphs (Hope et al. 2001). It is also sensitive to the presence of mineral-bound polyatomic ions such as carbonate (Griffith 1970). Raman spectroscopy can be applied to a petrographic thin section without any additional sample treatment or preparation, and each Raman spectrum provides a "fingerprint" which can often be unambiguously and uniquely matched to reference mineral spectra, even when phases are intimately intermixed (Carey et al. 2015). When fast, hyperspectral Raman mapping is combined with multivariate statistical analyses and a database of Raman mineral spectra such as the RRUFF database (Lafuente et al. 2015), maps of the distribution of mineral phases can be readily generated (e.g. Miller et al. 2016).

Raman hyperspectral images were acquired using a Horiba LabRAM HR Evolution Raman spectrometer with a 100 mW 532 nm excitation laser. The laser was focused through a 50x 0.75 NA dry objective onto the surface of the petrographic thin section. A 50% neutral density filter was used in order to attenuate the laser power and avoid damage to the sample,

resulting in approximately 14 mW of laser power at the sample surface focused to a ~2 μm spot. The sample was scanned under the ~2 μm laser spot with a 2 μm step size. At each pixel, two Raman spectra accumulated over 0.6 s were averaged. A 100 μm confocal pinhole and a 600 lines/mm diffraction grating were used to acquire the Raman spectrum with a spectral resolution of ~4.5 cm^{-1}. The confocal pinhole also limits the depth of Raman analysis to ~5 μm. Mapping in this way was repeated in order to acquire spectra for both the fingerprint region of the spectrum (85-1785 cm^{-1}) and the OH region of the spectrum (2800-3800 cm^{-1}). Each segment of the hyperspectral map dataset (fingerprint region and OH region) was individually area-normalized and corrected for instrumental artifacts before a polynomial baseline was subtracted using LabSpec 6 (Horiba Scientific). The datasets containing the two spectral regions, collected over the same map area, were then merged into a single hyperspectral dataset spanning the broader range of Raman shifts. Spectral endmembers were extracted from the map dataset using the multivariate curve resolution (MCR) feature of the software package SOLO-MIA (Eigenvector Research). MCR decomposes the hyperspectral map dataset into loading spectra and score maps. Non-negativity constraints on both the loadings and scores, appropriate for Raman hyperspectral data, help achieve a realistic solution where the loading spectra reflect actual mineral species present in the map (Andrew and Hancewicz 1998). Mineral phases were identified by searching the end-member spectra against the RRUFF database (Lafuente et al. 2015).

Synchrotron X-ray analysis

Fe redox calibration standards. Standards containing 100% octahedrally-coordinated Fe(II) (olivine and siderite), 100% octahedrally-coordinated Fe(III) (staurolite), 100% tetrahedrally-coordinated Fe(III) (sanidine), and a mixture of octahedrally coordinated Fe(II) and

Fe(III) (andradite) were generously provided by Manuel Muñoz (see Muñoz et al. 2013). These standards were used to calibrate the Fe redox variogram. We also used well-characterized materials (two chlorite specimens and one clintonite specimen), with known intermediate values of Fe(III)/∑Fe determined by Mossbauer, wet chemistry, and scanning transmission X-ray microscopy, as additional "standards" to validate the redox calibration and estimate calibration error (see error analysis section). These chlorite and clintonite samples were generously provided by Franck Bourdelle (Bourdelle et al. 2013).

Beamline setup. X-ray analyses were conducted using Beamline 2-3 at the Stanford Synchrotron Radiation Lightsource. The SPEAR3 ring was operated at 3 GeV with a current of 495-500 mA. Incident energy was selected using a water-cooled Si (111) $\phi = 0°$ double crystal monochromator. The Si(111) monochromator crystal was chosen to prioritize high flux for fast mapping (since we do not fit peak shapes to the pre-edge peak, high spectral resolution was not required). Kirkpatrick-Baez mirrors were used to microfocus the beam to an approximately 2.5 μm spot at the sample surface. The thin section sample was scanned across the X-ray beam at a 45° angle of incidence using a 2 μm step size. X-ray fluorescence was detected perpendicular to the X-ray beam (and at a 45° angle to the sample surface) using a single-element Si drift detector. The detector has extremely high throughput, but all fluorescence counts were corrected for deadtime (measured deadtime $\tau = 85$ ns using the paralyzable model, yielding a correction of < 5% for the highest count rates observed in the map).

Map data collection. Fe XRF maps were collected at 9 excitation energies across the pre-edge peak, plus one energy above the K edge, in order to generate an Fe(III)/∑Fe map. These

10 energies (7109.00, 7110.10, 7111.20, 7112.30, 7113.40, 7114.20, 7114.80, 7115.80, 7117.20, and 7200.00 eV) were chosen by inspecting a suite of >100 XANES spectra collected from serpentinite rocks on BL 2-3 and selecting energies that would capture the variation of pre-edge peak features and provide consistent baseline subtraction results. At Beamline 2-3, each horizontal row of the map is scanned at all 10 energies before moving on to the next row, which helps to minimize beam drift between maps of different energies, and thus the registration of the maps at each energy did not need to be adjusted (cf. Marcus 2010). The maps were collected with a 2 μm motor step size. A dwell time of 90 ms per pixel per energy was selected, which resulted in typical signal levels of 200 - 2000 counts on Fe per pixel in the pre-edge region and 10,000 - 30,000 counts on Fe per pixel above the edge. In this way, an area of 582 μm x 340 μm on the sample could be mapped in approximately 11 hours (because the sample is mounted at a 45° angle, motor steps of 2 μm give a pixel size of about 2 μm x 2.83 μm on the sample surface).

XANES spectroscopy data collection. XANES spectra spanning the full Fe K-edge feature (6882 eV – 7505 eV) were collected on 12 points within the map area to provide additional information about the Fe-speciation in the sample. Full XANES spectra were also collected on 5 endmember redox standards and 3 intermediate redox standards to facilitate calibration and validation of the Fe redox map. Spectra were collected with 0.10 eV steps within the pre-edge region from 7108.00 eV to 7118.00 eV. The dwell time was 3 s per point within the pre-edge region (7108.00 eV-7118.00 eV) and 1 s across the rest of the spectrum, requiring more than 10 minutes per spectrum for acquisition. Throughout the run, spectra were collected on Fe metal foil to monitor calibration drift. These spectra were collected with 5 s dwell time and 0.1 eV steps to precisely measure the position of the first inflection point (defined as 7112.00 eV).

240

241 **Energy Calibration.** To correct for drift in the energy calibration of the beamline, maps
242 and XANES spectra were calibrated using the first inflection point of Fe foil at 7112.00 eV.
243 Offsets were determined by calculating the first inflection point (maximum of the first
244 derivative) of a smoothing spline fit to the measured foil spectrum and computing the difference
245 from the defined value of 7112.00 eV. Fe foil offsets from foil measurements bracketing the data
246 collection of maps and XANES were averaged, and the maps and XANES spectra were then
247 shifted by this average offset. The calibrated centroid energy of Fe(II) and Fe(III) were measured
248 as 7112.88 eV and 7114.53 eV, respectively, in good agreement with the values reported
249 elsewhere (e.g. Giuli et al. 2012).

250

251 **Data Reduction**

252 Calculation of the Fe(III)/∑Fe maps was completed using in-house data analysis scripts
253 written in R (R Core Team 2018). All of the data and analysis code has been made available (see
254 Supplementary Information). These scripts handle the energy calibration, normalization, baseline
255 subtraction, peak integration, and variogram calculations described below.

256

257 **Pre-edge peak analysis of multiple energy maps.** We treated the fluorescence
258 intensities measured in each pixel at 10 different energies analogously to a XANES spectrum in
259 order to extract the pre-edge peak centroid position and integrated intensity. XRF maps were
260 normalized to the incoming beam intensity measured by an ion chamber (I_0), and then to the
261 XRF map collected at 7200.00 eV, an approximation of the edge step height (Figure 1A). One
262 point below 7112.00 eV and one point above 7112.00 eV were selected, such that an exponential

This is a preprint, the final version is subject to change, of the American Mineralogist (MSA)
Cite as Authors (Year) Title. American Mineralogist, in press.
DOI: https://doi.org/10.2138/am-2020-7359

baseline fit through these points falls below all other measured pre-edge points. This exponential baseline was subtracted from the normalized intensities, and the points not falling between the two selected baseline points were excluded from further analyses since they are not a part of the pre-edge peak feature (Figure 1B). The remaining points representing the pre-edge peak were then integrated to determine the pre-edge peak intensity and centroid position (Figure 1C). Figure 1 A-C also show a full-resolution XANES spectrum collected at the same spot in the map for comparison. In order to reduce random errors in the estimates of the pre-edge peak centroid and intensity, the 2D maps of centroid and intensity were smoothed by a gaussian filter ($\sigma = 1$ pixel).

Pre-edge peak analysis of XANES spectra. In order to construct an accurate calibration of the Fe(III)/∑Fe for the map dataset, the XANES spectra of the calibration standards are subjected to identical procedures for normalization, baseline subtraction, and integration. The full energy resolution of the XANES spectrum was used. Thus, fluorescence intensity was normalized to I_0 and to the intensity at 7200.00 eV. Single points below and above 7112.00 eV were selected as baseline points so that an exponential baseline fit through these points falls below all other measurements between 7108.00 eV and 7118.00 eV. The exponential baseline was subtracted from the normalized pre-edge intensities, and the points falling between the baseline points were then integrated to determine the pre-edge peak intensity and centroid position. XANES spectra collected within the map area of the sample were also treated identically to the map in order to facilitate direct comparison.

Variogram Adjustment. We reproduced the pre-edge peak variogram of Andreani *et al.* (2013) (which itself is modified from Wilke et al. 2001) by collecting pre-edge spectra of the same siderite, olivine, staurolite, andradite, and sanidine standards. To correct for differences in beamline setup and energy calibration, a transformation was applied by computing a linear regression between the values measured by Andreani *et al.* (2013) and our own measurements of the standards, for both the centroid position and integrated intensity. The linear transformation was then applied to the variogram of Andreani *et al.* (2013) in order to adapt the variogram to our measurements. It should be noted that the position of the variogram corners, in terms of centroid position and integrated intensity, varies somewhat depending on the average site geometry and symmetry of the standards (c.f. Giuli et al. 2011)

Variogram interpolation and redox estimation of maps. The Fe(III)/∑Fe tielines applicable for mixtures of ^{VI}Fe(II), ^{VI}Fe(III), and ^{IV}Fe(III) were adjusted to fit our end-member measurements using the same transformations as the standards. To calculate the Fe(III)/∑Fe ratio at the measured centroid and integrated intensity, the Fe(III)/∑Fe ratio was interpolated between the tielines using bivariate interpolation functions in the Akima package (Akima and Gebhardt 2016) and with the algorithm described by Renka (1996) (Figure 1D).

This method assumes that no ^{IV}Fe(II) is present in the sample, a reasonable assumption for all of the minerals encountered within our map area. Normal spinel structures, such as chromite, would have been the most likely ^{IV}Fe(II)-bearing mineral in this partially serpentinized peridotite, but this was not present within the map area. Minor amounts of ^{IV}Fe(II) could cause Fe(III)/∑Fe to be somewhat underestimated. Significant amounts of ^{IV}Fe(II) would result in the point falling above the ^{VI}Fe(II)-^{IV}Fe(III) join on the variogram, preventing the estimation of

This is a preprint, the final version is subject to change, of the American Mineralogist (MSA)
Cite as Authors (Year) Title. American Mineralogist, in press.
DOI: https://doi.org/10.2138/am-2020-7359

Fe(III)/∑Fe instead of resulting in a highly erroneous Fe(III)/∑Fe estimate. We do not attempt to quantify the average coordination number, which could be complicated by the possible presence of 5-fold coordinated Fe.

Co-registration

In order to explore the relationships between Fe redox state and mineral components, the Raman map and the pre-edge peak multiple-energy XRF maps were co-registered to each other. A transformation linking the two coordinate systems was found so that pixels in one map were matched to corresponding pixels at the same location on the sample in the other map. Four control points were selected using the TiO_2 (anatase) Raman map and the Ti XRF map. An affine transformation, allowing for translation, rotation, stretching, and shearing between the two maps was calculated from the control points. Bicubic interpolation was then used to resample the Raman map onto a grid in the coordinate system of the XRF Fe redox map. While the hard X-rays used in the XRF mapping (and the resulting Fe Kα fluorescence) likely penetrate the whole thickness of the thin section (~30 μm) (Lanzirotti et al. 2017), the confocal Raman map has an analysis depth limited to ~5 μm, which also varies according to the optical transparency of the minerals at the laser wavelength. In addition, the 45° geometry of the beamline introduces some mixing in the x direction. Still, it was possible to use co-registration to identify separate distributions of Fe(III)/∑Fe in different mineral phases.

This is a preprint, the final version is subject to change, of the American Mineralogist (MSA)
Cite as Authors (Year) Title. American Mineralogist, in press.
DOI: https://doi.org/10.2138/am-2020-7359

Results

Characterization of Sample OM14-07

Mantle rocks currently exposed at the surface in the Samail ophiolite in the Sultanate of Oman have experienced multiple stages of hydration at variable temperatures and fluid compositions (Mayhew et al., 2018). In this study, optical examination of the partially-serpentinized harzburgite OM14-07 that was sampled from a surface outcrop suggests that there is an intriguing mixture of primary and alteration phases with a potentially wide range of Fe redox states (Figure 2). Relict olivine is rimmed by an orange phase that appears likely to incorporate Fe(III), all in a matrix of serpentine with a small amount of magnetite. The Raman hyperspectral map corroborates these observations (Figure 3). Relict olivine is present with lizardite and chrysotile (two polymorphs of serpentine) in a mesh texture. Pyroaurite, an Fe(III)-bearing layered double hydroxide mineral ($Mg_6Fe_2^{3+}(OH)_{16}(CO_3) \cdot 4\,H_2O$), was also detected rimming some of the olivine crystals and filling mesh cores in association with a hydroxide phase. The hydroxide phase exhibits the Raman peaks of brucite around 280 cm^{-1}, 440 cm^{-1}, and 3630 cm^{-1}, but it also has a doublet peak around 550-600 cm^{-1}, which is not attributable to brucite, and this Raman spectrum extracted from the map could not be matched to any mineral Raman spectra in the RRUFF database. Finally, titanium dioxide (anatase) is shown in the fiducial marks and epoxy from thin section preparation is also detected. The observed mineral assemblage (i.e. olivine, pyroaurite) is suggestive of a strong redox contrast in this map area. Yet, no information could be gleaned as to the distribution of oxidation states of Fe in serpentine or the hydroxide phase from the Raman map alone.

Quantitative electron microprobe imaging reveals the elemental composition of the mineral phases identified by optical petrography and Raman spectroscopy (Figure 4). Olivine

This is a preprint, the final version is subject to change, of the American Mineralogist (MSA)
Cite as Authors (Year) Title. American Mineralogist, in press.
DOI: https://doi.org/10.2138/am-2020-7359

and serpentine are silicate minerals, whereas the areas identified as pyroaurite and the hydroxide phase are clearly SiO_2-free. The Fe map shows the distribution of mostly fine-grained magnetite within serpentine, and shows that pyroaurite and the hydroxide phase are Fe-rich relative to serpentine and olivine. Minor Ni and Cl are associated with the pyroaurite and hydroxide phase. The Mg map illustrates that the hydroxide phase is associated with significantly higher Mg than pyroaurite, whereas the Fe contents are similar. Thus, a map of the Mg# (molar proportion Mg/(Mg+Fe)) shows a higher Mg# for hydroxide than for pyroaurite. The approximate end-member compositions of these phases, extracted from regions of the EPMA map by averaging pixels, are summarized in Table 1.

Microscale synchrotron-based XRF mapping revealed a clear contrast in Fe pre-edge peak centroid and integrated intensity between different minerals in the sample. Calculations after normalization and baseline subtraction yield a centroid position and integrated intensity of the Fe pre-edge peak for every pixel in the map (Figure 5). Fe pre-edge peaks for olivine pixels have much lower centroid positions than serpentine, the hydroxide phase, or pyroaurite. Olivine Fe pre-edge features also have a relatively low integrated intensity. Small spinel grains (magnetite) have relatively high integrated Fe pre-edge peak intensity, while serpentine, pyroaurite, and the hydroxide phase exhibit intermediate intensities. Errors in the estimation of the centroid (0.1 eV) and intensity (0.007) of the Fe pre-edge peak were greatly improved by applying a gaussian smoothing filter to these maps (0.03 eV for the centroid and 0.003 for the intensity), and while this smoothing slightly degrades the effective spatial resolution of the image, it is an important step for improving the Fe redox quantification. The unsmoothed centroid and intensity maps are provided in Supplementary Information Figure 1.

372 The distribution of the pixel density that results from plotting the centroid and intensity
373 calculated at every pixel on the Fe variogram illustrates that four end-member Fe valence and
374 coordination states exist in the sample (Figure 6): (1) an octahedral Fe(II) endmember, which
375 likely corresponds to olivine; (2) a mixed-valence endmember containing significant $^{[IV]}$Fe(III)
376 having low abundance that likely corresponds to magnetite; (3) a mostly-octahedral Fe(III)
377 phase; and (4) a mostly octahedral endmember centered around 85% Fe(III)/∑Fe. Serpentine, the
378 hydroxide phase, and pyroaurite are likely associated with endmembers 3 and 4, but the correct
379 assignment of these minerals is not evident based on Figures 5 and 6 alone.
380 While magnetite contains equal parts $^{[6]}$Fe(II), $^{[6]}$Fe(III), and $^{[4]}$Fe(III), it typically plots
381 above the $^{[6]}$Fe(II)-$^{[4]}$Fe(III) join on the Fe variogram (c.f. Wilke et al. 2001). This anomalously
382 high integrated intensity associated with magnetite could potentially be caused by a combination
383 of several effects: (a) cation substitution by Cr and/or Ti leading to displacement of Fe(II) into
384 the tetrahedral sites (Wilke et al. 2001; Pearce et al. 2010), (b) overabsorption due to the high
385 density of Fe in magnetite (see below, "Analysis of Fe(III)/∑Fe Quantification Errors" for a
386 discussion of the effect of overabsorption), and (c) additional contributions to the pre-edge peak
387 caused by longer-range interactions of the photoelectron with surrounding atoms which can
388 occur in Fe oxides (Wilke et al. 2001). The exact Fe(III)/∑Fe, which is likely very close to 67%,
389 is not of particular interest in this study. Any error in the determination of Fe(III)/∑Fe that might
390 be introduced by these factors is mitigated by the fact that the calculation is invalidated when the
391 integrated intensity increases above the $^{[6]}$Fe(II)-$^{[4]}$Fe(III) join on the Fe variogram.
392 The Fe(III)/∑Fe ratio was calculated for every pixel based on where it plots relative to
393 the tielines on the variogram. These values are then depicted in a spatially resolved manner,
394 resulting in a map of the Fe redox state in terms of Fe(III)/∑Fe (Figure 7A). This map illustrates

the reduced nature of the relict olivine especially near the cores of the olivine crystals, with a transition to more intermediate redox at the olivine rim. The areas of the map that contain spinel phases and serpentine are also intermediate in Fe redox. Finally, the most oxidized areas of the map are the mesh cores containing pyroaurite and the hydroxide phase.

The Fe fluorescence map excited above the Fe K-edge at 7200 eV (shown in Figure 5A) is a proxy for the Fe concentration. Thus, it is possible to multiply this fluorescence signal by the Fe(III)/∑Fe to determine the amount of fluorescence due to Fe(III), and by 1-(Fe(III)/∑Fe) for the amount of fluorescence due to Fe(II). These values can then be mapped to green and red color intensities in order to construct a composite map of Fe(II) and Fe(III) distribution (Figure 7B). Phases which contain a relatively high concentration of Fe(II) appear in bright green, and this map demonstrates clearly that olivine is the dominant host of Fe(II). In contrast, the pyroaurite and hydroxide phase in the mesh cores appear to incorporate the majority of Fe(III) present in the sample, as shown in bright red. This map also underscores that while serpentine contains both Fe(II) and Fe(III), it is not Fe-rich (the low Fe concentration is represented by the dark color), and hence it is not a major host of either Fe(II) or Fe(III).

While visually correlating the Fe redox maps with the Raman mineralogy maps gives helpful insight into the distribution of Fe(II) and Fe(III) among the mineral phases, it is possible to combine these datasets in order to quantify the Fe redox of each mineral phase by merging the Fe redox and the Raman mineralogy maps. The two maps were projected into the same coordinate system by matching features of the TiO_2 fiducial marks in both maps and calculating an appropriate transformation (Supplementary Information Figure 3). This allows the Raman mineralogy map to be interpolated onto the Fe redox map grid, resulting in paired Raman-Fe(III)/∑Fe data at each pixel. Information from one map (mineral identification from the Raman

map) can be layered onto the data in the other (Fe(III)/∑Fe in the Fe redox map). Pixels representative of distinct mineral phases can then be individually identified on the Fe variogram (Figure 8A). The minerals separate into different regions of the variogram, reflecting their unique Fe speciation. The spread in the distributions reflect the uncertainty in the Fe(III)/∑Fe quantification, mixed analyses, and miscategorization of the minerals, as well as any natural variation that may exist within each mineral phase (Figure 8B). Pixels dominated by an olivine signal in the Raman map, and thus classified as olivine, span a wide range in Fe(III)/∑Fe, from 0% to ~60%, which is likely due to a combination of mixed-phase analyses, particularly in pixels that include fine-scale olivine weathering products, and/or small errors in the co-registration process. Serpentine is concentrated between 65% and 85% Fe(III)/∑Fe. The hydroxide phase is the most oxidized phase in the map, with Fe(III)/∑Fe ranging from 90 to 100%. Finally, pyroaurite separates into two populations of pixels, with the majority ranging from 70% to 100% Fe(III)/∑Fe, overlapping with serpentine and the hydroxide phase. A smaller portion of the pixels overlaps with the most oxidized olivine pixels (45% to 60% Fe(III)/∑Fe). The larger population of more oxidized pyroaurite pixels are associated with mesh cores containing pyroaurite and hydroxide phase, while the more reduced pyroaurite pixels were found in the pyroaurite rim around olivine.

Analysis of Fe(III)/∑Fe Quantification Errors

The error associated with the Fe redox quantifications shown in Figures 6 and 7 was estimated as a combination of errors from several sources. The underlying Fe variogram method of Wilke et al. (2001), which was applied to mineral powders, has an inherent error of ±10% Fe(III)/∑Fe, which accounts for errors and uncertainties associated with the different mineral

441 structures, extraction of the centroid and intensity through peak fitting, variogram calibration,
442 and energy drift of the beam.

443 An additional source of error is necessarily introduced when this technique is applied at
444 the microscale, since the observed XANES spectrum and pre-edge peak shapes of anisotropic
445 minerals depend on crystallographic orientation relative to the polarization direction of the X-ray
446 beam (Dyar et al. 2001, 2002a; Muñoz et al. 2013; Evans et al. 2014; Dyar et al. 2016b). Since
447 we cannot control for these orientation effects when mapping across many mineral grains in a
448 thin section, these effects manifest as errors in our Fe(III)/∑Fe measurement. The magnitude of
449 the orientation error is mineral-dependent, but data is available for only a few minerals. Muñoz
450 et al. (2013) showed that orientation effects could cause Fe(III)/∑Fe to be underestimated by up
451 to 10% or overestimated by up to 5% for antigorite, which is probably a good approximation for
452 the serpentine-group minerals, chrysotile and lizardite, we observed. Since the magnitude of the
453 orientation effects for olivine, pyroaurite, hydroxide phase, etc. are not known, we have extended
454 the measurements of Muñoz et al. (2013) for antigorite to all of the minerals in our sample,
455 acknowledging that there may be additional error in those measurements. We discuss the
456 sensitivity of the overall error to stronger orientation effects below. Muñoz et al. (2013) shows
457 that the error follows a sine function with the orientation angle, and it is important to note that
458 for a random uniform distribution of orientations, this leads to error with an arcsine probability
459 distribution between -10% and 5%, so that the more extreme errors near -10% and 5% are
460 somewhat more probable than smaller absolute errors (Supplementary Information Figure 4).

461 The error due to the coarse sampling of the XANES spectrum and our background fitting
462 and pre-edge peak integration techniques was determined by comparing the results of these
463 procedures to those of the classical approaches (e.g. Bajt et al. 1994; Galoisy et al. 2001; Wilke

et al. 2001) on 12 full XANES spectra collected within the OM14-07 sample plus three replicate spectra collected on each of a set of 3 well-characterized materials provided by F. Bourdelle (two chlorite specimens and one clintonite specimen which were not used in calibrating the variogram). Manual peak fitting was performed using Athena (Ravel and Newville 2005) with the background modelled by a smoothing spline fit through the data several eV below and above the pre-edge peak. The pre-edge peak was fit with gaussian peak shapes, and the heights, widths, and centroid positions were allowed to float. A separate variogram was calibrated for this approach, based on standard spectra treated analogously. The spectra were then also down-sampled to the 10 energies used in mapping, and treated analogously to the redox map including the baseline fitting and centroid/integrated intensity calculation approaches. The treatment of variogram calibration standards differed only in that the spectra were not down-sampled to the 10 mapped energies as the "sample" spectra were, since the full resolution of the standard spectra is also used to calibrate the variogram applied to the Fe(III)/∑Fe redox map. The Fe(III)/∑Fe determined for these spectra are compared in Figure 9a. Our approach to determining the Fe(III)/∑Fe, applied to spectra that were down-sampled to the energies measured in the map dataset, was able to reproduce the Fe(III)/∑Fe measured from the full resolution spectrum with a complex baseline and peak-fitting, with an error of ± 6.2%. Furthermore, while only three known "standards" were evaluated, the Fe(III)/∑Fe measured using our approach on the down-sampled spectra of the chlorite and clintonite specimens was close to the known value, with a root mean squared error (RMSE) of ± 9.8% (Figure 9b), consistent with the ±10% error associated with the original variogram method (Wilke et al. 2001).

We used Monte Carlo simulations to propagate the uncertainty associated with the counting statistics of our short dwell time through to the centroid position, integrated intensity,

and Fe(III)/∑Fe quantification. For every fluorescence measurement (i.e. at every pixel and every excitation energy), we simulated 200 new fluorescence measurements by randomly sampling a Poisson distribution with parameter λ equal to the fluorescence that was actually observed. We then repeated the whole procedure for determining the Fe(III)/∑Fe on the simulated maps, which resulted in a simulated distribution composed of 200 Fe(III)/∑Fe estimates at each pixel. This error due to shot noise led to errors of ±0.10 eV on the pre-edge peak centroid and ±0.0067 on the pre-edge peak intensity (note that these error estimates for shot noise should not be interpreted as the total uncertainty on the centroid or integrated intensity). However, this was significantly reduced, to ±0.03 eV and ± 0.0026 on the centroid energy and intensity respectively, by the gaussian smoothing filter applied to the centroid and intensity maps prior to the Fe(III)/∑Fe determination. Thus, the Fe(III)/∑Fe error due to shot noise was ±3.2% overall. These errors are a function of the Fe fluorescence counts, and are therefore greater for Fe-poor minerals or pixels.

When XANES spectra are collected in fluorescence, overabsorption (often called self-absorption) can occur if the sample is thick or relatively concentrated in the element being measured. The main effect of overabsorption in the context of our dataset would be to decrease the fluorescence measured above the edge at 7200 eV. Upon normalization to this value, the fluorescence along the pre-edge region would appear higher than it would for an appropriately thin or dilute sample, and this would cause the measured integrated intensity of the pre-edge peak to increase.

We modeled the effects of overabsorption on the map using theoretical equations for overabsorption in samples of finite thickness (Haskel 1999; Booth and Bridges 2005) and the tables of absorption coefficients of Hubbell and Seltzer (2009). The equations account for the

beamline geometry (45° angle between the beam and the sample, 45° between the sample and the detector), sample composition, and sample thickness. We considered four different chemical compositions: serpentine (Mg# 0.96 based on the EPMA results), olivine (Mg# 0.90), pyroaurite (ideal formula; $Mg_6Fe_2(OH)_{16}CO_3 \cdot 4\ H_2O$), and magnetite (ideal formula; Fe_3O_4). For serpentine, olivine, and pyroaurite, we assumed the thickness of the sample was 30 μm. Due to the high density of Fe in magnetite, this phase has the potential to cause strong overabsorption. Magnetite is present mostly as fine, dispersed grains, thus we assumed a typical thickness for magnetite of 3 μm, for which the over-absorption would be smaller. Since the over absorption estimates for each mineral composition considered for this sample were similar, they were pooled to estimate the overall error from over absorption.

The results of the simulation show that overabsorption was minimal in the sample we studied. Because of the density of Fe, magnetite would have been the phase most affected by overabsorption. While one larger grain of magnetite was present in the map area, and the overabsorption effect was large enough to push the integrated intensity of those pixels above the $^{[VI]}$Fe(II)-$^{[IV]}$Fe(III) join, this was isolated to a small number of pixels (shown in magenta in Figure 7). Since the Fe(III)/∑Fe values were invalidated for those pixels, it did cause erroneous Fe(III)/∑Fe estimates. Calculations for olivine, serpentine, and pyroaurite with a thickness of 30 μm, and for magnetite with a thickness of 3 μm, indicate that overabsorption could have caused the integrated intensity to increase by 0.01 ± 0.005, whereas the centroid energy would have been unchanged (0.000 ± 0.002 eV). The over-estimated intensity, in turn, would have caused Fe(III)/∑Fe to be underestimated by 1% ± 1%. Thus, overabsorption contributes negligible error compared to the other factors we considered.

This is a preprint, the final version is subject to change, of the American Mineralogist (MSA)
Cite as Authors (Year) Title. American Mineralogist, in press.
DOI: https://doi.org/10.2138/am-2020-7359

The error on the Fe(III)/∑Fe measurement of each pixel in our map is a combination of the errors from the various sources discussed above, but because they are not all normally distributed (especially the error due to orientation effects, which is asymmetric and has a complex arcsine distribution), they cannot be simply added in quadrature. Monte Carlo simulation of the total error based on random sampling of the component error distributions leads to a total uncertainty of ±14% Fe(III)/∑Fe (RMSE). The mean error is -2%, due to a slight systematic bias introduced by the asymmetry of the errors from orientation and overabsorption. Using the more severe orientation effects measured for biotite, which are associated with an error with a total range of -15% to 10% Fe(III)/∑Fe (Muñoz et al. 2013; in general agreement with Dyar et al. 2001, 2002a), increases the total RMSE to ±15% Fe(III)/∑Fe (the systematic bias increases to -3%). Finally, we note that this error analysis gives the uncertainty of the Fe(III)/∑Fe value derived for a single pixel in the map. A portion of this error can be averaged out when considering larger groups of pixels, such as those belonging to various minerals as shown in Figure 8.

This is a preprint, the final version is subject to change, of the American Mineralogist (MSA)
Cite as Authors (Year) Title. American Mineralogist, in press.
DOI: https://doi.org/10.2138/am-2020-7359

Discussion

Characterization of Oman serpentinite using Fe redox mapping

Understanding the evolution of Fe redox state in hydrated peridotites is key to unraveling the sequence of Fe transformations that have occurred and determining the timing, temperature, and probability of H_2 production. The oxidation of Fe(II) derived from primary minerals to form Fe(III)-bearing secondary minerals can be coupled to the reduction of water and the release of H_2, with important implications for habitability (e.g. Sleep et al. 2004; McCollom and Bach 2009). Fe(II) originally released during hydration of olivine (or other primary minerals such as pyroxene) is partitioned among a variety of Fe-bearing secondary minerals with a wide range of Fe redox states, including awaruite (Fe^0), brucite (Fe^{2+}), serpentine minerals (variable Fe^{2+} and Fe^{3+}), magnetite (1 Fe^{2+} : 2 Fe^{3+}), and a variety of Fe(II-III)-(hydr)oxides (variable Fe^{2+} and Fe^{3+}). These reactions often occur over several episodes of alteration and are responsive to many aspects of the evolving mineral assemblage and fluid chemistry. Determining how Fe has been partitioned among the various extant mineral phases is a key step to deciphering the sequence of mineral transformations and variety of reaction conditions (including temperature, oxygen fugacity, and water:rock ratio), particularly with respect to Fe redox behavior during mineral alteration and hydration (Andreani et al. 2013; McCollom et al. 2016; Mayhew et al. 2018). The finely intergrown textures of several of the Fe-bearing minerals such as serpentine and brucite necessitates a microscale approach to quantifying Fe redox state, because the presence of Fe(III) in the serpentine structure is an important signal that H_2 production could have occurred, whereas the diversion of Fe(II) for the formation of brucite is not associated with H_2 production (McCollom and Bach 2009; Klein et al. 2014).

Application of the Fe redox mapping approach we developed has enabled us to identify key changes in Fe speciation and valence during serpentinization and weathering reactions in the Oman ophiolite. Surface outcrop sample OM14-07 from the Oman ophiolite is a partially serpentinized peridotite that has likely undergone multiple episodes of water/rock interaction, including during hydrothermal circulation on the seafloor and during obduction (Neal and Stanger 1985; Streit et al. 2012; Bonnemains et al. 2016). Each of the mineral phases observed in OM14-07 can incorporate Fe in one or more of its valence states. The mesh-textured serpentine hosts cores of relict olivine rimmed by pyroaurite. However, many of the mesh cores lack olivine and are completely replaced by a mixture of pyroaurite and a hydroxide phase. The close association of pyroaurite with olivine is suggestive of a sharp redox gradient within this sample because pyroaurite is Fe(III)-rich while olivine is a primary Fe(II)-bearing mineral. Still, without making direct measurements of Fe(III)/∑Fe it is difficult to infer the redox state of Fe in many of the multi-valent phases present in this sample, especially serpentine and the hydroxide phase.

Olivine was the most reduced mineral phase in the map area. The quantification of Fe(III)/∑Fe values in pixels where the Raman spectrum shows olivine to be the dominant phase spans a broad range of 0-60%. Olivine is known to accommodate very little Fe(III), therefore the oxidized pixels observed here must not reflect Fe within primary olivine. Some of this spread likely represents an overlap of olivine and Fe(III) bearing minerals in the XRF analysis volume (especially given the presence of pyroaurite immediately rimming the olivine). The beamline geometry is such that the incident X-ray beam encounters the sample at a 45° angle, and the analysis depth of the XRF Fe(III)/∑Fe dataset is much greater than that of the confocal Raman mineralogy dataset, all of which could create situations where mixed analyses are collected even in locations where the Raman spectrum is very pure. Additionally, inaccuracies in the co-

591 registration of the redox and Raman maps and/or miscategorization of mixed pixels as olivine in
592 the Raman map could contribute to the wide distribution of observed Fe(III)/∑Fe in olivine.
593 Areas of the map containing olivine appear to have strongly reduced cores and more oxidized
594 rims, which would be consistent with mixed analyses near the edges of the olivine grains causing
595 the more oxidized values. Finally, it is also possible that additional oxidized weathering products
596 of olivine have formed and were not detected except through their oxidized Fe signature (perhaps
597 in submicrometer channels within the olivine, e.g. Banfield et al., 1990).

598 Serpentine minerals are known to incorporate significant amounts of Fe(II) and/or Fe(III)
599 (Evans et al. 2009; Andreani et al. 2013; Beard and Frost 2016). Using only optical and Raman
600 observations, the Fe(III)/∑Fe of serpentine in this sample was entirely unconstrained, however
601 the accommodation of Fe(III) into serpentine could play an important role in facilitating H_2
602 production (Andreani et al. 2013; Klein et al. 2014) in the magnetite-poor rocks typical of the
603 Oman ophiolite (Bonnemains et al. 2016). Additionally, it is of interest to know the range and
604 distribution of Fe(III)/∑Fe for serpentine, since multiple generations of serpentine might occur
605 with Fe redox (Andreani et al. 2013). Our results demonstrate that although the lizardite and
606 chrysotile in this sample are Fe-poor compared to olivine, pyroaurite, and the hydroxide phase,
607 they have a distinct intermediate Fe redox composition, around 65-85% Fe(III)/∑Fe. The
608 observed Fe(III)/∑Fe of the chrysotile/lizardite mixture is consistent with measurements of
609 Fe(III)/∑Fe of lizardite and/or chrysotile from other settings determined by Mössbauer
610 spectroscopy (O'Hanley and Dyar 1993, 1998; Votyakov et al. 1993; O'Hanley and Wicks 1995;
611 Klein et al. 2009; Evans et al. 2012; Greenberger et al. 2015; Mayhew and Ellison 2020). In
612 general, lizardite tends to accommodate a greater proportion of Fe(III) than chrysotile does
613 (O'Hanley 1996; O'Hanley and Dyar 1998; Mayhew and Ellison 2020), but there is no clear

relationship between the dominant serpentine polymorph and Fe(III)/∑Fe within the map area, at least at the resolution of the Raman and redox maps (Figures 3 and 7). Small grains of magnetite are present within serpentine in the map area in some places, and can be seen as opaque minerals in Figure 2 and as small regions with elevated Fe fluorescence and integrated intensity in Figure 5. Since the nominal Fe(III)/∑Fe of magnetite is 67%, it is possible that Fe in magnetite is responsible for some of the lower Fe(III)/∑Fe pixels in the distribution of serpentine; however, we expect the number of affected pixels to be small.

We detected a Fe-bearing hydroxide phase which we have not been able to further identify. Its Raman spectrum includes the major peaks observed in Raman spectra of brucite (278 cm^{-1}, 444 cm^{-1}, and 3640 cm^{-1}) and indicates the presence of hydroxyl groups (Lutz et al. 1994). EPMA analyses show that this phase contains major Mg and Fe and no appreciable Si, while the low analytical total suggests major H_2O, CO_2, or other volatiles. The EPMA analysis was most consistent with Fe-bearing brucite, although the total is lower than would be expected for Fe(II)-substituted brucite (for example, $Mg_{0.82}Fe_{0.18}(OH)_2$ would contain 28.1% H_2O and would be expected to give an analytical total of 71.9%, but this phase has a total of only 64.6%, suggesting that it contains up to 35.4% H_2O). However, the Raman spectrum could not be matched to any mineral in the RRUFF database due to the presence of additional Raman peaks not found in the spectrum of brucite (doublet between 540 cm^{-1} and 620 cm^{-1}), nor could it be modeled as a mixture of multiple Raman spectra such as brucite and an Fe(III)-(hydr)oxide mineral. Since the identity of this phase was unknown, so too was its Fe redox state. Understanding the redox state is likely valuable information to aid in elucidating the structure and origin of this puzzling mineral phase. Since this phase was intimately mixed with pyroaurite,

it would have been difficult to select locations to collect pure individual XANES spectra or know which spectra were most representative of this phase.

The Fe redox mapping approach revealed that the hydroxide phase is quite Fe(III)-rich, having a high normalized Fe fluorescence signal and Fe(III)/∑Fe > 90%. Brucite is a common product of serpentinization of olivine, and significant Fe(II) is known to substitute for Mg in the brucite structure, but much less Fe(III) (perhaps up to ~10% Fe(III)/∑Fe; Beard and Frost 2016). Thus, the high Fe(III) content supports our conclusion that the hydroxide phase is mineralogically distinct from brucite. However, the Fe(III) does not seem to be incorporated in an Fe(III)-(hydr)oxide structure, based on the Raman spectrum (Faria et al. 1997; Hanesch 2009). We infer that it is likely a Mg-Fe(III)-hydroxide phase, perhaps with a layered double hydroxide structure composed of trioctahedral brucite-like sheets bearing net positive charge, which is balanced by interlayer anions. Many of the Raman peaks in the hydroxide phase spectrum could be explained by such a layered double hydroxide structure, with the feature at 620 cm^{-1} remaining notably unexplained. Unlike pyroaurite, it does not appear to contain any carbonate since no C-O stretch band is observed around 1070 cm^{-1} in the Raman spectrum. Since there is little Cl or S associated with this phase, the interlayer anion might possibly be OH^-, such as in the layered double hydroxide mineral muskoxite (approximate formula $Mg_7Fe_4^{3+}(OH)_{26} \cdot 4H_2O$), which remains incompletely characterized in general and for which we are not aware of a published Raman spectrum (Jambor 1969; Mills et al. 2012).

Pyroaurite is an important host of Fe(III) in the observed alteration assemblage. The structure of pyroaurite (as well as the related Mg-Fe-CO_3 hydrotalcite-group minerals brugnatellite and coalingite) is composed of brucite sheets, substituted with Fe(III), with intercalated carbonate ions balancing the excess positive charge of the brucite sheets (Hansen

659 and Koch 1995). On the basis of this structural similarity, pyroaurite could be thought of as an
660 oxidized and partially carbonated form of brucite. Pyroaurite has been described associated with
661 serpentinite from Oman, and is often associated with near-surface weathering of brucite-bearing
662 serpentinites (Mumpton and Thompson 1975; Taylor et al. 1991; Boschi et al. 2017). Pyroaurite
663 is likely able to incorporate some Fe(II) through substitution for Mg^{2+} in the brucite sheets
664 corresponding to a solid solution with a green rust carbonate end-member, which has an
665 analogous layered double hydroxide structure and is known to incorporate Mg^{2+} (Refait et al.
666 2001; Feder et al. 2005).

667 While Fe(III)/∑Fe of pixels dominated by pyroaurite span a wide range from 45% to
668 100%, much of this variation could be due to mixed analyses. The most reduced values are
669 associated with pyroaurite rims around olivine and therefore could be influenced by Fe(II) in
670 olivine. Most of the pyroaurite was not associated with olivine, but instead was associated with
671 the more oxidized hydroxide phase, and was therefore unlikely to be significantly influenced by
672 Fe(II) in neighboring phases. This pyroaurite was found to contain around 75% - 95%
673 Fe(III)/∑Fe, suggesting the presence of minor Fe(II) in the pyroaurite structure.

674

675 **Insights into serpentinization processes in the Oman ophiolite**

676 The sample we examined is partially serpentinized, and has likely been subjected to
677 multiple stages of serpentinization. One or more earlier stages of serpentinization may have
678 produced the chrysotile veins throughout the investigated area, which include minor magnetite.
679 The most recent stage of serpentinization likely occurred at relatively low temperatures, and
680 produced lizardite and Fe-rich brucite (which was consumed by subsequent reactions) in rims
681 around olivine and in mesh cores lacking olivine. The mesh-rim zonation with brucite forming a

682 rim between the olivine core and the serpentine of the outer rim has been described by Klein et
683 al. (2009), who concluded that this indicated a strong gradient in silica activity from the olivine-
684 brucite reaction front to the intergranular fluid with a higher SiO_2 activity derived from
685 serpentinization of orthopyroxene.

686 We suggest that Fe(II)-brucite, first produced from the hydration of olivine, later became
687 oxidized during reaction in the near-surface environment with an oxidizing, carbonate-bearing
688 fluid, producing both pyroaurite and the Fe(III)-bearing hydroxide phase. This oxidation could
689 have occurred in the shallow aquifer observed in the Oman ophiolite (Neal and Stanger 1983,
690 1985; Miller et al. 2016; Rempfert et al. 2017), or during subaerial weathering by meteoric water
691 when the sample was exposed at the outcrop. This two-stage reaction sequence is consistent with
692 interpretations of layered double hydroxide mineral occurrence after Fe-rich brucite in other
693 serpentinized rocks (Heling and Schwarz 1992; Bach et al. 2004; Boschi et al. 2017), and with
694 the well-known reaction producing Fe-rich brucite during olivine hydration (Frost and Beard
695 2007; McCollom and Bach 2009). However, we cannot rule out the possibility that the hydration
696 of olivine occurred under oxidizing conditions, directly producing pyroaurite and the oxidized
697 hydroxide phase.

698 If Fe(II)-rich brucite was initially formed as we suggest, this implies that it would have
699 occurred under reducing conditions. At least a portion of the serpentine in the sample would have
700 formed contemporaneously with the brucite to accommodate SiO_2 released by olivine, and we
701 assume that the serpentine within our map area is representative of the Fe(III)/$\sum$Fe of this
702 relatively recent generation of serpentine. Thus, oxidation of Fe incorporated into that serpentine
703 may have occurred via reduction of water and production of H_2.

Measurements of Fe(III)/∑Fe have allowed us to identify two main stages of reaction that have led to the Fe speciation observed in sample OM14-07. Serpentinization of primary olivine, potentially in multiple stages, lead to the concurrent formation of serpentine and abundant, Fe-rich brucite. We infer that this reaction occurred under reducing conditions because a large proportion of Fe(II) liberated from olivine was sequestered into Fe(II)-brucite. This Fe(II) played no role in H_2 production. However, approximately 70% of the Fe incorporated into the serpentine was oxidized to Fe(III), and this oxidation of Fe could have contributed to the formation of H_2. Subsequently, upon exhumation and weathering by oxidizing, CO_2-bearing shallow groundwater and/or meteoric fluids, the Fe-rich brucite further reacted to form a mixture of pyroaurite and an oxidized hydroxide phase. If O_2 or other oxidants other than water were present and participated by oxidizing the Fe, these reactions would not result in the production of H_2.

Comparison to other methods for measuring microscale Fe(III)/∑Fe

While there are several other approaches available for the microscale determination of Fe redox state, no other approach would have allowed us to access all of the information contained in the Fe redox image. Electron energy loss spectroscopy (EELS) (van Aken and Liebscher 2002; Cavé et al. 2006; Kim and Dong 2011) and scanning transmission X-ray microscopy (STXM) (Bourdelle et al. 2013; Elmaleh et al. 2015) have nanoscale spatial resolution, which is required in certain systems where nanoscale mineral intergrowths and redox variations are under investigation. However, both require sample preparation for a transmission-mode experiment, and the area that is interrogated is limited to a few square micrometers or less. X-ray photo-emission electron microscopy (XPEEM) allows qualitative Fe(III)/∑Fe mapping, and can be combined with quantitative microscale spot analyses on thin section samples (De Stasio et al.

2001; Schofield et al. 2014), but we are not yet aware of any demonstration of truly quantitative Fe redox mapping with XPEEM. Conventional Mössbauer spectroscopy has allowed spot analyses of Fe redox at the milliscale (McCammon 1994; McCammon et al. 2001), while recent advances in synchrotron Mössbauer spectroscopy have permitted microscale analyses of Fe redox (Potapkin et al. 2012; Yan et al. 2012), but neither technique has yet been optimized for mapping Fe redox state. Similarly, a method of determining Fe redox state by analyzing the Fe $L_{2,3}$ edges by electron microprobe (e.g. Höfer et al. 1994) requires a wavelength scan that is time-consuming and has not been adapted to mapping.

Electron microprobe analysis (EMPA) can be used to quantify redox state by assuming a specific mineral stoichiometry to calculate charge-balance (e.g. Droop 1987). The EMPA charge balance approach has been adapted to quantitative mapping of Fe redox in some geological samples by focusing on a single mineral for which stoichiometric charge balance is well-constrained (Vidal et al. 2006), but this approach would be difficult to apply to a complex mineral assemblage, especially one that includes minerals without rigid stoichiometric constraints for Fe substitution, such as serpentine (Beard and Frost 2016).

Fe redox mapping has previously been achieved using XANES approaches related to the method we have described. Multiple energy mapping at the Fe K-edge has been applied with excellent precision to garnets in a peridotite xenolith by Berry et al. (2013). The excitation energies they selected and the intensity ratio they calculated for quantitative Fe(III)/∑Fe mapping was specifically designed for garnets and is not applicable to other minerals. Using a synchrotron beamline equipped with dispersive optics that allow a full XANES spectrum to be quickly collected at each mapping pixel, the position of the main Fe K-edge has been mapped as a proxy for Fe(III)/∑Fe (Muñoz et al. 2006). Though their hyperspectral datasets do include the

pre-edge peak, these authors focus on the position of the main-edge position to generate a qualitative Fe redox map, which they compare to a second quantitative map derived from EMPA and charge-balance calculations. A similar approach based on a dispersive setup and the main-edge position was used by Andreani et al. (2013) to qualitatively image Fe redox and applied to a serpentinite with complex Fe chemistry.

The multiple energy mapping approach using the Fe pre-edge peak that we present here fills a critical gap in our current capabilities. Each alternative method has provided valuable information in the studies in which they have been applied and there is certainly the potential for further improvements and development. However, none of these techniques could have provided the quantitative Fe(III)/∑Fe map of a microscale area containing a diversity of Fe-bearing minerals in a standard petrographic thin section.

Limitations of method

The technique for determining Fe redox based on the Fe pre-edge peak has been the subject of many developments since it was first applied by Bajt et al. (1994). One important contribution was the introduction of the Fe variogram by Wilke et al. (2001), accounting for varying pre-edge peak intensity depending on coordination number, which affects the relative contribution to the pre-edge peak centroid. Other important developments include the development of mineral-specific calibrations (e.g. Dyar et al., 2012), studies of the crystal orientation effects on the pre-edge peak and redox estimate (e.g. Dyar et al. 2002a; Muñoz et al. 2013), and the application of new multivariate statistical approaches (e.g. Dyar et al. 2016a, 2016b; Marcus et al. 2008).

This is a preprint, the final version is subject to change, of the American Mineralogist (MSA)
Cite as Authors (Year) Title. American Mineralogist, in press.
DOI: https://doi.org/10.2138/am-2020-7359

As with any X-ray based technique, there is potential for photo-oxidation of Fe caused by heating under the X-ray beam (Brown and Sturchio 2002). Debret et al. (2014) characterized the effect of beam damage on the pre-edge peak centroid position of serpentine, and found a shift of the centroid to higher energies of ~0.13 eV and ~0.07 eV, resulting in an over-estimation of Fe(III)/∑Fe of less than 10% and 5% for antigorite and lizardite respectively over a period of 25 minutes of exposure. Cottrell et al. (2018) showed that beam damage can occur quickly in hydrous glasses, over timescales of just a few minutes, and depend on the X-ray photon flux. Though these characterizations were performed on different beamlines with different beam characteristics, we expect the effect of beam damage on the redox mapping results to be insignificant because of the way the maps are collected. Each pixel receives a series of 10 exposures lasting only 90 ms each, with several seconds between the exposures, as one row of the map is scanned at each excitation energy before advancing to the next row. Still, it is important to be aware of this potential complication because the sensitivities of other minerals to beam damage are unknown.

Since our method relies on the variogram calibration of Wilke et al. (2001), our method is subject to the constraints of that method. The variogram allows mixtures of three Fe redox/coordination endmembers to be calibrated, and the version of the Fe variogram we applied is calibrated for mixtures of ^{VI}Fe(II), ^{VI}Fe(III), and ^{IV}Fe(III) only. This assumption is valid for all of the phases detected in our sample. Fe(III)/∑Fe quantification using the variogram approach may be impossible if more than three Fe redox-coordination combinations are present in the phases of interest in a given sample (Wilke et al. 2001).

We have shown that an appropriate baseline can be fit to the pre-edge peak, and the entire pre-edge peak can be integrated to determine the centroid and integrated intensity required for

the redox determination. However, because our approach does not involve the least-squares fitting of peak shapes to the pre-edge peak (e.g. with software such as ATHENA, Ravel and Newville 2005), which is not feasible with the small number of points that can be measured during mapping, it is limited to materials that do not contain additional pre-edge peak components. This includes phases like hematite and ferrihydrite, Fe(III) phases with pre-edge peak features falling at higher energies than those used in the Fe(III)/∑Fe calibration. These peaks would interfere with the baseline fitting and Fe(III)/∑Fe determination in our method. It may be possible to apply the Fe(III)/∑Fe mapping approach in samples containing such phases if they are assumed to contain only Fe(III) and are not the phases of interest. However, care must be taken to ensure that these phases are not intergrown with the phases of interest since they would significantly bias the Fe(III)/∑Fe measurement.

For the highest accuracy in Fe(III)/∑Fe quantification, it is clear that mineral-specific calibrations should be performed; in other words, samples should be compared to a set of standards of the same mineral phase with a range of Fe(III)/∑Fe. Studies that have compared the calibrations determined for different mineral groups (or chemical compositions of glasses), or compared mineral specific calibrations to general calibrations like those of Bajt et al. (1994), have shown that differences do exist (Dyar et al. 2001; Cottrell et al. 2009; Speicher et al. 2011). However, the more general calibrations allow multiple minerals (or mixtures) to be examined simultaneously, which is required for the type of mapping demonstrated in the current work. Thus, it is appropriate to apply the general calibration of Wilke et al. (2001) in this method, with appropriate care for its limitations and to account for its inherent uncertainty.

Recently, more precision in Fe(III)/∑Fe quantification has been achieved using redox information contained in the regions of the spectrum at and above the main Fe K-edge (as

818 opposed to the pre-edge peak). Berry et al. (2010) reported a calibration for garnets (which are
819 isotropic, and thus do not suffer from orientation effects) based on the post-edge intensity ratio at
820 7138.4 eV and 7161.7, with stated errors of ±1% Fe(II)/∑Fe. Dyar et al. (2016a) used
821 multivariate statistical models trained on the whole XANES spectrum to predict Fe(III)/∑Fe of
822 silicate glasses with stated errors of ±3.4%. A similar multivariate approach applied to garnets
823 (Dyar et al. 2012) yielded a model with a stated error of ±6.9% Fe(III)/∑Fe and performed better
824 than the intensity ratio technique of Berry et al. (2010). When applied to anisotropic minerals,
825 these multivariate statistical techniques taking into account the full spectrum have also been
826 shown to perform better than techniques using the pre-edge peak. By collecting spectra from
827 oriented single crystals of amphibole, it was possible to predict the Fe(III)/∑Fe of crystals with
828 the same orientation with errors better than ±1% (depending on orientation and model type);
829 when predicting randomly oriented crystals the error was ±5.5-6.2% (Dyar et al. 2016b). Clearly,
830 the edge and post edge regions contain additional information on Fe valence state that cannot be
831 extracted via the traditional pre-edge peak techniques. These studies show great promise for
832 developing mineral-specific Fe(III)/∑Fe calibrations with increased accuracy with applicability
833 to quantitative mapping. Still, these techniques are currently only applicable to individual
834 mineral groups due to the strong confounding effects of mineral species on XANES spectrum
835 structure; no such model is available that can be applied to a range of several mineral phases
836 within a map area as shown here.

837 Crystal orientation relative to the propagation and polarization directions of the X-ray
838 beam is known to affect both the observed XANES spectrum structure as well as the pre-edge
839 peak centroid and intensity, and is a significant source of error in the Fe(III)/∑Fe quantification
840 reported here. Orientation effects on Fe redox estimates have been studied for a variety of

This is a preprint, the final version is subject to change, of the American Mineralogist (MSA)
Cite as Authors (Year) Title. American Mineralogist, in press.
DOI: https://doi.org/10.2138/am-2020-7359

minerals (Dyar et al. 2001, 2002a; Muñoz et al. 2013; Evans et al. 2014; Dyar et al. 2016b). In the case of antigorite, Fe(III)/∑Fe could be underestimated by 10% or overestimated by 5%, an effect that is somewhat smaller than other phyllosilicate minerals such as talc and biotite (Muñoz et al. 2013). Serpentine crystallites in thin-section may be poorly-oriented to well-oriented on the scale of the X-ray spot size (Boudier et al. 2010; Andreani et al. 2013), which potentially reduces the magnitude of errors due to orientation within serpentine. Dyar et al. (2002b) noted changes in pre-edge peak shape for olivine but did not elaborate on orientation dependence of the centroid or intensity of the feature. Other minerals, including pyroaurite and the hydroxide phase, are likely impacted by orientation effects of unknown magnitude. For thin section samples, crystallographic orientation will be difficult to control when undertaking redox mapping. Through mapping, we interrogate many different crystals, some of which may have different orientations, which would have the effect of partially averaging out orientation effects in the sample overall. It may be possible to mitigate the errors associated with orientation through future method development. Evans et al. (2014) attempted to use electron back-scatter diffraction (EBSD) to measure the crystallographic orientation of biotite in thin section in order to apply a correction to Fe(III)/∑Fe measured by μXANES but encountered difficulty producing an effective correction model; still, this approach seems very promising. Multivariate statistical models trained on oriented single crystal standards (Dyar et al. 2016b) may also provide a means of eliminating this error source.

Pre-edge redox mapping as a powerful tool to discern Fe valence state

We combined the existing techniques of multiple energy X-ray fluorescence mapping and Fe-redox quantification with the Fe variogram to develop a method for microscale Fe redox

mapping. By collecting XRF maps at multiple energies across the pre-edge peak, we were able to reconstruct the shape and size of the pre-edge peak across more than 34,000 pixels. We developed an algorithm for finding a suitable baseline using this small number of measurements per pixel and were able to determine the centroid and integrated intensity at every pixel in the map. Based on a carefully calibrated Fe variogram and the centroid and intensity measurements, we quantified the Fe redox state in each pixel, expressed as the Fe(III)/∑Fe ratio. We also combined the Fe fluorescence map collected above the edge which qualitatively measures the distribution of total Fe within the map area to depict the relative amount of Fe(II) and Fe(III) among the various mineral phases present in the map area. Finally, we combined the Fe redox map dataset with a hyperspectral Raman mineralogical map to assess the oxidation state variability of each distinct mineral identified, even when some of these phases were intimately mixed at the microscale.

Extending Fe redox quantification beyond microscale selected spot-analyses to generate fully quantitative maps provides a detailed rendering of the complex spatial variation of Fe valence state. Images provide spatially continuous information in two dimensions. Locations within the area of interest that contain spectral, mineralogical, redox, or atomic-coordination endmembers are inevitably captured in the dataset, whereas the identification and analysis of endmembers is a primary challenge for discrete-point datasets (Mayhew et al. 2011).

The redox mapping technique we have developed allows the pre-edge feature to be reconstructed with sufficient fidelity to provide a quantitative Fe(III)/∑Fe measurement without a major sacrifice of precision, despite the high speed of analysis per pixel. We propagated error due to measurement noise through each of the required steps for constructing the Fe redox map, and showed that the Fe(III)/∑Fe can be determined with a precision of ± 3.2% Fe(III)/∑Fe. The

This is a preprint, the final version is subject to change, of the American Mineralogist (MSA)
Cite as Authors (Year) Title. American Mineralogist, in press.
DOI: https://doi.org/10.2138/am-2020-7359

largest source of imprecision originates from the down-sampling of the pre-edge feature (fluorescence only measured at nine energies), and this could potentially be improved by mapping at additional energies. The workflow we describe includes the collection of full XANES spectra with high-resolution and relatively low signal:noise across the pre-edge peak, which provides an element of "ground truthing" to verify the accuracy of Fe(III)/∑Fe quantification. We estimate the overall uncertainty from all sources to be ± 14% absolute Fe(III)/∑Fe.

The spatially continuous Fe redox map datasets are readily combined with maps derived from complementary techniques by co-registering maps collected over the same sample region. We demonstrated that a complementary mineralogy map derived from Raman hyperspectral imaging could be leveraged to extract the distribution of Fe(III)/∑Fe measurements associated with each mineral phase. This allowed the unique Fe(III)/∑Fe signatures of serpentine and the hydroxide phase to be identified, which allow us to interpret a sequence of Fe transformations associated with serpentinization and weathering.

The value of the method we have described is enhanced because it will be relatively simple to implement at a variety of microfocused hard X-ray beamlines available at many synchrotron facilities worldwide. Dispersive X-ray optics have been used to generate qualitative Fe redox maps (e.g. Muñoz et al., 2006; Andreani et al., 2013), but these setups are uncommon and therefore more difficult to access. The simplicity of implementing our method on a variety of beamlines is likely to facilitate its application to a wide variety of scientific applications by a larger group of researchers.

Important Considerations for Method Implementation

This is a preprint, the final version is subject to change, of the American Mineralogist (MSA)
Cite as Authors (Year) Title. American Mineralogist, in press.
DOI: https://doi.org/10.2138/am-2020-7359

This method should provide researchers with an accessible way to image and elucidate redox gradients in complex materials. Several brief suggestions are provided to help facilitate the implementation of this approach. First, it is critical to consider whether the information this method is able to provide is appropriate to the question under investigation. The spatial scale and achievable spatial resolution, uncertainty of quantification, and the scale of the expected redox contrasts in the samples are all important factors to take into account. With respect to the practical implementation of the methods, it is important to acquire high-quality standards both for calibration of the variogram, and ideally also for subsequent verification of the calibration. Researchers should aim to match the mineral structure and chemical composition of "internal standards" with known Fe(III)/∑Fe to phases expected to be present in the samples, if possible. Finally, it is important that researchers reconsider the errors quantified in the present work, and any other sources that may be important for a particular application, to determine whether their contributions to the overall uncertainty might differ significantly from what was evaluated here.

Temporal beamline drift can be very problematic. If the energy of the beam drifts, even by small fractions of an eV, it will severely hamper the Fe(III)/∑Fe. Measurements of an energy standard such as Fe foil many times throughout a run is critical to correcting for energy drift. Similarly, if the focal point of the beam moves relative to the sample, it could necessitate additional co-registration of the XRF maps.

The fluorescence signal needs to be sufficient for good counting statistics; good results were obtained in this study with approximately 100,000 counts per second on Fe above the edge. The dynamic range of the fluorescence detector should also be considered, since some detectors will have much larger deadtime corrections. Additionally, the sample should be evaluated for the

This is a preprint, the final version is subject to change, of the American Mineralogist (MSA)
Cite as Authors (Year) Title. American Mineralogist, in press.
DOI: https://doi.org/10.2138/am-2020-7359

931 severity of potential overabsorption. If there are phases with high densities of the element of
932 interest, a very thin sample may be required for best results.

933 Collecting high-resolution XANES spectra, especially on end-member phases identified
934 through mapping, can help in deciphering the variation in the map. These spectra can also be
935 utilized to "ground-truth" the observed Fe(III)/∑Fe in the map.
936

This is a preprint, the final version is subject to change, of the American Mineralogist (MSA)
Cite as Authors (Year) Title. American Mineralogist, in press.
DOI: https://doi.org/10.2138/am-2020-7359

Implications

Redox reactions involving Fe are integral to biogeochemical processes, including in soil, freshwater, and marine, sediment, hard-rock, and engineered environments. These Fe redox reactions often occur at interfaces such as mineral surfaces, and the reaction products can be heterogeneous on the microscale. A method for determining the redox state of Fe of natural materials are required to interrogate these processes. This analysis must be conducted at the spatial scale of the individual phases present in a solid sample, and is most useful if the analysis can be done on a standard petrographic thin section or grain mount, which can also be analyzed with numerous other optical and spectroscopic techniques. The spatially continuous information contained in a Fe redox image provides additional insight that spot analyses of Fe redox cannot.

While several methods exist for probing Fe redox on the microscale, the methods that are capable of image-mode analysis of redox are limited and may require involved sample preparation and/or uncommon experimental setups. Our method can be applied to a standard petrographic thin section, and the resulting maps can be merged with map datasets derived from Raman spectroscopy, EMPA chemical mapping, or other microscale imaging techniques. Our method can be used at any synchrotron beamline set up for microfocused hard X-ray fluorescence spectroscopy and mapping, of which there are many worldwide, which should allow Fe redox imaging to become a relevant technique on a wide variety of geological and environmental samples.

This is a preprint, the final version is subject to change, of the American Mineralogist (MSA)
Cite as Authors (Year) Title. American Mineralogist, in press.
DOI: https://doi.org/10.2138/am-2020-7359

957 **Acknowledgments**

958 We thank Manuel Muñoz and Franck Bourdelle for providing mineral specimens with
959 known Fe valence and coordination. We thank SSRL staff scientists Sam Webb and Courtney
960 Krest for their assistance with the synchrotron XRF and XAS analyses. We thank Aaron Bell for
961 assistance with EPMA analyses. We thank Sebastian Kopf for assistance with R code. We
962 appreciate the suggestions from Mathew Marcus, M. Rita Cicconi, and three anonymous
963 reviewers, which greatly improved the manuscript.

964 Use of the Stanford Synchrotron Radiation Lightsource, SLAC National Accelerator
965 Laboratory, is supported by the U.S. Department of Energy, Office of Science, Office of Basic
966 Energy Sciences under Contract No. DE-AC02-76SF00515. Raman and EPMA analyses were
967 performed at the Raman Microspectroscopy Laboratory and the Electron Microprobe
968 Laboratory, respectively, at the Department of Geological Sciences, University of Colorado-
969 Boulder. This work was funded by the Rock Powered Life NASA Astrobiology Institute
970 (Cooperative Agreement NNA15BB02A).

971

This is a preprint, the final version is subject to change, of the American Mineralogist (MSA)
Cite as Authors (Year) Title. American Mineralogist, in press.
DOI: https://doi.org/10.2138/am-2020-7359

References

Akima, H., and Gebhardt, A. (2016) akima: Interpolation of Irregularly and Regularly Spaced Data.

Andreani, M., Muñoz, M., Marcaillou, C., and Delacour, A. (2013) µXANES study of iron redox state in serpentine during oceanic serpentinization. Lithos, 178, 70–83.

Bach, W., Garrido, C.J., Paulick, H., Harvey, J., and Rosner, M. (2004) Seawater-peridotite interactions: First insights from ODP Leg 209, MAR 15°N. Geochemistry, Geophysics, Geosystems, 5, Q09F26.

Bajt, S., Sutton, S.R., and Delaney, J.S. (1994) X-ray microprobe analysis of iron oxidation states in silicates and oxides using X-ray absorption near edge structure (XANES). Geochimica et Cosmochimica Acta, 58, 5209–5214.

Banfield, J.F., Veblen, D.R., and Jones, B.F. (1990) Transmission electron microscopy of subsolidus oxidation and weathering of olivine. Contributions to Mineralogy and Petrology, 106, 110–123.

Beard, J.S., and Frost, B.R. (2016) The stoichiometric effects of ferric iron substitutions in serpentine from microprobe data. International Geology Review, 1–7.

Berry, A.J., Danyushevsky, L.V., St C. O'Neill, H., Newville, M., and Sutton, S.R. (2008) Oxidation state of iron in komatiitic melt inclusions indicates hot Archaean mantle. Nature, 455, 960–963.

Berry, A.J., Yaxley, G.M., Woodland, A.B., and Foran, G.J. (2010) A XANES calibration for determining the oxidation state of iron in mantle garnet. Chemical Geology, 278, 31–37.

Berry, A.J., Yaxley, G.M., Hanger, B.J., Woodland, A.B., Jonge, M.D. de, Howard, D.L., Paterson, D., and Kamenetsky, V.S. (2013) Quantitative mapping of the oxidative effects of mantle metasomatism. Geology, 41, 683–686.

Bonnemains, D., Carlut, J., Escartín, J., Mével, C., Andreani, M., and Debret, B. (2016) Magnetic signatures of serpentinization at ophiolite complexes. Geochemistry, Geophysics, Geosystems, 17, 2969–2986.

Booth, C.H., and Bridges, F. (2005) Improved self-absorption correction for fluorescence measurements of extended x-ray absorption fine-structure. Physica Scripta, 2005, 202–204.

Boschi, C., Dini, A., Baneschi, I., Bedini, F., Perchiazzi, N., and Cavallo, A. (2017) Brucite-driven CO2 uptake in serpentinized dunites (Ligurian Ophiolites, Montecastelli, Tuscany). Lithos, 288–289, 264–281.

Boudier, F., Baronnet, A., and Mainprice, D. (2010) Serpentine mineral replacements of natural olivine and their seismic implications: Oceanic lizardite versus subduction-related antigorite. Journal of Petrology, 51, 495–512.

Bourdelle, F., Benzerara, K., Beyssac, O., Cosmidis, J., Neuville, D.R., Brown, G.E., and Paineau, E. (2013) Quantification of the ferric/ferrous iron ratio in silicates by scanning transmission X-ray microscopy at the Fe L2,3 edges. Contributions to Mineralogy and Petrology, 166, 423–434.

Brown, G.E., and Sturchio, N.C. (2002) An overview of synchrotron radiation applications to low temperature geochemistry and environmental science. Reviews in Mineralogy and Geochemistry, 49, 1–115.

Brown, G.E., Calas, G., Waychunas, G., and Petiau, J. (1988) X-Ray Absorption Spectroscopy: Applications in Mineralogy and Geochemistry. In F. Hawthorne, Ed., Spectroscopic methods in mineralogy and geology Vol. 18, pp. 431–512. Mineralogical Society of America.

Buss, H.L., Sak, P.B., Webb, S.M., and Brantley, S.L. (2008) Weathering of the Rio Blanco quartz diorite, Luquillo Mountains, Puerto Rico: Coupling oxidation, dissolution, and fracturing. Geochimica et Cosmochimica Acta, 72, 4488–4507.

Calas, G., and Petiau, J. (1983) Coordination of iron in oxide glasses through high-resolution K-edge spectra: Information from the pre-edge. Solid State Communications, 48, 625–629.

Carey, C., Boucher, T., Mahadevan, S., Bartholomew, P., and Dyar, M.D. (2015) Machine learning tools for mineral recognition and classification from Raman spectroscopy. Journal of Raman Spectroscopy, 46, 894–903.

Cavé, L., Al, T., Loomer, D., Cogswell, S., and Weaver, L. (2006) A STEM/EELS method for mapping iron valence ratios in oxide minerals. Micron, 37, 301–309.

Colombo, C., Palumbo, G., He, J.-Z., Pinton, R., and Cesco, S. (2014) Review on iron availability in soil: Interaction of Fe minerals, plants, and microbes. Journal of Soils and Sediments, 14, 538–548.

Cottrell, E., and Kelley, K.A. (2011) The oxidation state of Fe in MORB glasses and the oxygen fugacity of the upper mantle. Earth and Planetary Science Letters, 305, 270–282.

Cottrell, E., Kelley, K.A., Lanzirotti, A., and Fischer, R.A. (2009) High-precision determination of iron oxidation state in silicate glasses using XANES. Chemical Geology, 268, 167–179.

Cottrell, E., Lanzirotti, A., Mysen, B., Birner, S., Kelley, K.A., Botcharnikov, R., Davis, F.A., and Newville, M. (2018) A Mössbauer-based XANES calibration for hydrous basalt glasses reveals radiation-induced oxidation of Fe. American Mineralogist, 103, 489–501.

De Stasio, G., Gilbert, B., Frazer, B.H., Nealson, K.H., Conrad, P.G., Livi, V., Labrenz, M., and Banfield, J.F. (2001) The multidisciplinarity of spectromicroscopy: from geomicrobiology to archaeology. Journal of Electron Spectroscopy and Related Phenomena, 114–116, 997–1003.

Debret, B., Andreani, M., Muñoz, M., Bolfan-Casanova, N., Carlut, J., Nicollet, C., Schwartz, S., and Trcera, N. (2014) Evolution of Fe redox state in serpentine during subduction. Earth and Planetary Science Letters, 400, 206–218.

Droop, G.T.R. (1987) A general equation for estimating Fe3+ concentrations in ferromagnesian silicates and oxides from microprobe analyses, using stoichiometric criteria. Mineralogical Magazine, 51, 431–435.

Dyar, M.D., Delaney, J.S., and Sutton, S.R. (2001) Fe XANES spectra of iron-rich micas. European Journal of Mineralogy, 13, 1079–1098.

Dyar, M.D., Gunter, M.E., Delaney, J.S., Lanzarotti, A., and Sutton, S.R. (2002a) Systematics in the structure and XANES spectra of pyroxenes, amphiboles, and Micas as derived from oriented single crystals. The Canadian Mineralogist, 40, 1375–1393.

Dyar, M.D., Gunter, M.E., Delaney, J.S., Lanzirotti, A., and Sutton, S.R. (2002b) Use of the spindle stage for orientation of single crystals for microXAS: Isotropy and anisotropy in Fe-XANES spectra. American Mineralogist, 87, 1500–1504.

Dyar, M.D., Breves, E.A., Emerson, E., Bell, S.W., Nelms, M., Ozanne, M.V., Peel, S.E., Carmosino, M.L., Tucker, J.M., Gunter, M.E., and others (2012) Accurate determination of ferric iron in garnets by bulk Mössbauer spectroscopy and synchrotron micro-XANES. American Mineralogist, 97, 1726–1740.

Dyar, M.D., McCanta, M., Breves, E., Carey, C.J., and Lanzirotti, A. (2016a) Accurate predictions of iron redox state in silicate glasses: A multivariate approach using X-ray absorption spectroscopy. American Mineralogist, 101, 744–747.

Dyar, M.D., Breves, E.A., Gunter, M.E., Lanzirotti, A., Tucker, J.M., Carey, C.J., Peel, S.E., Brown, E.B., Oberti, R., Lerotic, M., and others (2016b) Use of multivariate analysis for synchrotron micro-XANES analysis of iron valence state in amphiboles. American Mineralogist, 101, 1171–1189.

Elmaleh, A., Bourdelle, F., Caste, F., Benzerara, K., Leroux, H., and Devouard, B. (2015) Formation and transformations of Fe-rich serpentines by asteroidal aqueous alteration processes: A nanoscale study of the Murray chondrite. Geochimica et Cosmochimica Acta, 158, 162–178.

Essilfie-Dughan, J., Hendry, M.J., Warner, J., and Kotzer, T. (2013) Arsenic and iron speciation in uranium mine tailings using X-ray absorption spectroscopy. Applied Geochemistry, 28, 11–18.

Etschmann, B.E., Ryan, C.G., Brugger, J., Kirkham, R., Hough, R.M., Moorhead, G., Siddons, D.P., De Geronimo, G., Kuczewski, A., Dunn, P., and others (2010) Reduced As components in highly oxidized environments: Evidence from full spectral XANES imaging using the Maia massively parallel detector. American Mineralogist, 95, 884–887.

Evans, B.W., Kuehner, S.M., and Chopelas, A. (2009) Magnetite-free, yellow lizardite serpentinization of olivine websterite, Canyon Mountain complex, N.E. Oregon. American Mineralogist, 94, 1731–1734.

Evans, B.W., Dyar, M.D., and Kuehner, S.M. (2012) Implications of ferrous and ferric iron in antigorite. American Mineralogist, 97, 184–196.

Evans, K.A., Dyar, M.D., Reddy, S.M., Lanzirotti, A., Adams, D.T., and Tailby, N. (2014) Variation in XANES in biotite as a function of orientation, crystal composition, and metamorphic history. American Mineralogist, 99, 443–457.

Farges, F., and Wilke, M. (2016) Planetary, geological and environmental sciences. In J.A. Van Bokhoven and C. Lamberti, Eds., X-Ray Absorption and X-Ray Emission Spectroscopy pp. 561–608. John Wiley & Sons, Ltd, Chichester, UK.

Faria, D.L.A. de, Silva, S.V., and Oliveira, M.T. de (1997) Raman microspectroscopy of some iron oxides and oxyhydroxides. Journal of Raman Spectroscopy, 28, 873–878.

Feder, F., Trolard, F., Klingelhöfer, G., and Bourrié, G. (2005) In situ Mössbauer spectroscopy: Evidence for green rust (fougerite) in a gleysol and its mineralogical transformations with time and depth. Geochimica et Cosmochimica Acta, 69, 4463–4483.

Frost, B.R., and Beard, J.S. (2007) On Silica Activity and Serpentinization. Journal of Petrology, 48, 1351–1368.

Galoisy, L., Calas, G., and Arrio, M.A. (2001) High-resolution XANES spectra of iron in minerals and glasses: structural information from the pre-edge region. Chemical Geology, 174, 307–319.

Giuli, G., Paris, E., Hess, K.-U., Dingwell, D.B., Cicconi, M.R., Eeckhout, S.G., Fehr, K.T., and Valenti, P. (2011) XAS determination of the Fe local environment and oxidation state in phonolite glasses. American Mineralogist, 96, 631–636.

Giuli, G., Cicconi, M.R., and Paris, E. (2012) The [4]Fe3+–O distance in synthetic kimzeyite garnet, Ca3Zr2[Fe2SiO12]. European Journal of Mineralogy, 24, 783–790.

Greenberger, R.N., Mustard, J.F., Cloutis, E.A., Pratt, L.M., Sauer, P.E., Mann, P., Turner, K., Dyar, M.D., and Bish, D.L. (2015) Serpentinization, iron oxidation, and aqueous conditions in an ophiolite: Implications for hydrogen production and habitability on Mars. Earth and Planetary Science Letters, 416, 21–34.

1109 Griffith, W.P. (1970) Raman studies on rock-forming minerals. Part II. Minerals containing MO3,
1110 MO4, and MO6 groups. Journal of the Chemical Society A: Inorganic, Physical,
1111 Theoretical, 286.

1112 Hanesch, M. (2009) Raman spectroscopy of iron oxides and (oxy)hydroxides at low laser power
1113 and possible applications in environmental magnetic studies. Geophysical Journal
1114 International, 177, 941–948.

1115 Hansen, H.C.B., and Koch, C.B. (1995) Synthesis and characterization of pyroaurite. Applied Clay
1116 Science, 10, 5–19.

1117 Haskel, D. (1999, May 27) FLUO: Correcting XANES for self absorption in fluorescence
1118 measurements. The Advanced Photon Source, Argonne National Laboratory.

1119 Heling, D., and Schwarz, A. (1992) Iowaite in serpentinite muds at Sites 778, 779, 780, and 784:
1120 a possible cause for the low chlorinity of pore waters. (P. Fryer, J.A. Pearce, L.B.
1121 Stokking, & et al., Eds.)Proceedings of the Ocean Drilling Program, Scientific Results,
1122 125, 313–323.

1123 Höfer, H.E., Brey, G.P., Schulz-Dobrick, B., and Oberhaensli, R. (1994) The determination of the
1124 oxidation state of iron by the electron microprobe. European Journal of Mineralogy, 6,
1125 407–418.

1126 Hope, G.A., Woods, R., and Munce, C.G. (2001) Raman microprobe mineral identification.
1127 Minerals Engineering, 14, 1565–1577.

1128 Hubbell, J.H., and Seltzer, S.M. (2009, September 17) NIST Standard Reference Database 126:
1129 Tables of X-ray mass attenuation coefficients and mass energy-absorption coefficients
1130 (version 1.4). National Institute of Standards and Technology.

1131 Jambor, J.L. (1969) Muskoxite, a new hydrous magnesium-ferric iron oxide from the Muskox
1132 Intrusion, Northwest Territories, Canada. American Mineralogist, 54, 684–696.

1133 Johnson, C.A., Freyer, G., Fabisch, M., Caraballo, M.A., Küsel, K., and Hochella, M.F. (2014)
1134 Observations and assessment of iron oxide and green rust nanoparticles in metal-
1135 polluted mine drainage within a steep redox gradient. Environmental Chemistry, 11,
1136 377–391.

1137 Kim, J., and Dong, H. (2011) Application of electron energy-loss spectroscopy (EELS) and energy-
1138 filtered transmission electron microscopy (EFTEM) to the study of mineral
1139 transformation associated with microbial Fe-reduction of magnetite. Clays and Clay
1140 Minerals, 59, 176–188.

1141 Klein, F., Bach, W., Jöns, N., McCollom, T., Moskowitz, B., and Berquó, T. (2009) Iron partitioning
1142 and hydrogen generation during serpentinization of abyssal peridotites from 15°N on
1143 the Mid-Atlantic Ridge. Geochimica et Cosmochimica Acta, 73, 6868–6893.

Klein, F., Bach, W., Humphris, S.E., Kahl, W.-A., Jöns, N., Moskowitz, B., and Berquó, T.S. (2014) Magnetite in seafloor serpentinite—Some like it hot. Geology, 42, 135–138.

Lafuente, B., Downs, R.T., Yang, H., and Stone, N. (2015) The power of databases: The RRUFF project. In T. Armbruster and R.M. Danisi, Eds., Highlights in mineralogical crystallography pp. 1–30. Walter de Gruyter GmbH, Berlin ; Boston.

Lam, P.J., Ohnemus, D.C., and Marcus, M.A. (2012) The speciation of marine particulate iron adjacent to active and passive continental margins. Geochimica et Cosmochimica Acta, 80, 108–124.

Lanzirotti, A., Sutton, S.R., Dyar, M.D., McCanta, M.C., and Head, E. (2017) Advances in high-resolution synchrotron micro-XANES for constraining the redox evolution of terrestrial and extraterrestrial magma. In AGU Fall Meeting Abstracts Vol. 53.

Le Guillou, C., Changela, H.G., and Brearley, A.J. (2015) Widespread oxidized and hydrated amorphous silicates in CR chondrites matrices: Implications for alteration conditions and H2 degassing of asteroids. Earth and Planetary Science Letters, 420, 162–173.

Lutz, H.D., Möller, H., and Schmidt, M. (1994) Lattice vibration spectra. Part LXXXII. Brucite-type hydroxides M(OH)2 (M = Ca, Mn, Co, Fe, Cd) — IR and Raman spectra, neutron diffraction of Fe(OH)2. Journal of Molecular Structure, 328, 121–132.

Marcus, M.A. (2010) X-ray photon-in/photon-out methods for chemical imaging. TrAC Trends in Analytical Chemistry, 29, 508–517.

Marcus, M.A., Westphal, A.J., and Fakra, S.C. (2008) Classification of Fe-bearing species from K-edge XANES data using two-parameter correlation plots. Journal of Synchrotron Radiation, 15, 463–468.

Mayhew, L.E., and Ellison, E.T. (2020) A synthesis and meta-analysis of the Fe chemistry of serpentinites and serpentine minerals. Philosophical Transactions of the Royal Society A: Mathematical, Physical and Engineering Sciences, 378, 20180420.

Mayhew, L.E., Webb, S.M., and Templeton, A.S. (2011) Microscale imaging and identification of Fe speciation and distribution during fluid–mineral reactions under highly reducing conditions. Environmental Science & Technology, 45, 4468–4474.

Mayhew, L.E., Ellison, E.T., Miller, H.M., Kelemen, P.B., and Templeton, A.S. (2018) Iron transformations during low temperature alteration of variably serpentinized rocks from the Samail ophiolite, Oman. Geochimica et Cosmochimica Acta, 222, 704–728.

McCammon, C.A. (1994) A Mössbauer milliprobe: Practical considerations. Hyperfine Interactions, 92, 1235–1239.

McCammon, C.A., Griffin, W.L., Shee, S.R., and O'Neill, H.S.C. (2001) Oxidation during metasomatism in ultramafic xenoliths from the Wesselton kimberlite, South Africa: implications for the survival of diamond. Contributions to Mineralogy and Petrology, 141, 287–296.

McCanta, M.C., Dyar, M.D., Lanzirotti, A., Newville, M., and Breitenfeld, L.B. (2019) In-situ mapping of ferric iron variations in lunar glasses using X-ray absorption spectroscopy. American Mineralogist, 104, 453–458.

McCollom, T.M., and Bach, W. (2009) Thermodynamic constraints on hydrogen generation during serpentinization of ultramafic rocks. Geochimica et Cosmochimica Acta, 73, 856–875.

McCollom, T.M., Klein, F., Robbins, M., Moskowitz, B., Berquó, T.S., Jöns, N., Bach, W., and Templeton, A. (2016) Temperature trends for reaction rates, hydrogen generation, and partitioning of iron during experimental serpentinization of olivine. Geochimica et Cosmochimica Acta, 181, 175–200.

Miller, H.M., Matter, J.M., Kelemen, P., Ellison, E.T., Conrad, M.E., Fierer, N., Ruchala, T., Tominaga, M., and Templeton, A.S. (2016) Modern water/rock reactions in Oman hyperalkaline peridotite aquifers and implications for microbial habitability. Geochimica et Cosmochimica Acta, 179, 217–241.

Mills, S.J., Christy, A.G., Génin, J.-M.R., Kameda, T., and Colombo, F. (2012) Nomenclature of the hydrotalcite supergroup: natural layered double hydroxides. Mineralogical Magazine, 76, 1289–1336.

Mino, L., Borfecchia, E., Groppo, C., Castelli, D., Martinez-Criado, G., Spiess, R., and Lamberti, C. (2014) Iron oxidation state variations in zoned micro-crystals measured using micro-XANES. Catalysis Today, 229, 72–79.

Mumpton, F.A., and Thompson, C.S. (1975) Mineralogy and Origin of the Coalinga Asbestos Deposit. Clays and Clay Minerals, 23, 131–143.

Muñoz, M., De Andrade, V., Vidal, O., Lewin, E., Pascarelli, S., and Susini, J. (2006) Redox and speciation micromapping using dispersive X-ray absorption spectroscopy: Application to iron in chlorite mineral of a metamorphic rock thin section. Geochemistry, Geophysics, Geosystems, 7, Q11020.

Muñoz, M., Vidal, O., Marcaillou, C., Pascarelli, S., Mathon, O., and Farges, F. (2013) Iron oxidation state in phyllosilicate single crystals using Fe-K pre-edge and XANES spectroscopy: Effects of the linear polarization of the synchrotron X-ray beam. American Mineralogist, 98, 1187–1197.

Myneni, S.C.B., Tokunaga, T.K., and Brown, G.E. (1997) Abiotic selenium redox transformations in the presence of Fe(II,III) oxides. Science, 278, 1106–1109.

Neal, C., and Stanger, G. (1983) Hydrogen generation from mantle source rocks in Oman. Earth and Planetary Science Letters, 66, 315–320.

Neal, C., and Stanger, G. (1985) Past And Present Serpentinisation of Ultramafic Rocks; An Example from the Semail Ophiolite Nappe of Northern Oman. In J.I. Drever, Ed., The Chemistry of Weathering Vol. 149, pp. 249–275. Springer Netherlands, Dordrecht.

O'Hanley, D.S. (1996) Serpentinites: Recorders of Tectonic and Petrological History, 290 p. Oxford University Press, Oxford, New York.

O'Hanley, D.S., and Dyar, M.D. (1993) The composition of lizardite 1T and, the formation of magnetite in serpentinites. American Mineralogist, 78, 391–404.

——— (1998) The composition of chrysotile and its relationship with lizardite. The Canadian Mineralogist, 36, 727–739.

O'Hanley, D.S., and Wicks, F.J. (1995) Conditions of formation of lizardite, chrysotile and antigorite, Cassiar, British Columbia. The Canadian Mineralogist, 33, 753–773.

O'Loughlin, E.J., Kelly, S.D., Cook, R.E., Csencsits, R., and Kemner, K.M. (2003) Reduction of uranium(VI) by mixed iron(II)/iron(III) hydroxide (green rust): formation of UO2 nanoparticles. Environmental Science & Technology, 37, 721–727.

Pearce, C.I., Henderson, C.M.B., Telling, N.D., Pattrick, R.A.D., Charnock, J.M., Coker, V.S., Arenholz, E., Tuna, F., and Laan, G. van der (2010) Fe site occupancy in magnetite-ulvöspinel solid solutions: A new approach using X-ray magnetic circular dichroism. American Mineralogist, 95, 425–439.

Potapkin, V., Chumakov, A.I., Smirnov, G.V., Celse, J.-P., Rüffer, R., McCammon, C., and Dubrovinsky, L. (2012) The 57Fe synchrotron Mössbauer source at the ESRF. Journal of Synchrotron Radiation, 19, 559–569.

Prietzel, J., Thieme, J., Eusterhues, K., and Eichert, D. (2007) Iron speciation in soils and soil aggregates by synchrotron-based X-ray microspectroscopy (XANES, μ-XANES). European Journal of Soil Science, 58, 1027–1041.

R Core Team (2018) R: A Language and Environment for Statistical Computing. R Foundation for Statistical Computing, Vienna, Austria.

Ravel, B., and Newville, M. (2005) ATHENA, ARTEMIS, HEPHAESTUS: data analysis for X-ray absorption spectroscopy using IFEFFIT. Journal of Synchrotron Radiation, 12, 537–541.

Refait, P., Abdelmoula, M., Trolard, F., Génin, J.-M.R., Ehrhardt, J.J., and Bourrié, G. (2001) Mössbauer and XAS study of a green rust mineral; the partial substitution of Fe2+ by Mg2+. American Mineralogist, 86, 731–739.

Rempfert, K.R., Miller, H.M., Bompard, N., Nothaft, D., Matter, J.M., Kelemen, P., Fierer, N., and Templeton, A.S. (2017) Geological and geochemical controls on subsurface microbial life in the Samail Ophiolite, Oman. Frontiers in Microbiology, 8.

Renka, R.J. (1996) Algorithm 751: TRIPACK: a constrained two-dimensional Delaunay triangulation package. ACM Transactions on Mathematical Software, 22, 1–8.

Schofield, P.F., Smith, A.D., Scholl, A., Doran, A., Covey-Crump, S.J., Young, A.T., and Ohldag, H. (2014) Chemical and oxidation-state imaging of mineralogical intergrowths: The application of X-ray photo-emission electron microscopy (XPEEM). Coordination Chemistry Reviews, 277–278, 31–43.

Sleep, N.H., Meibom, A., Fridriksson, T., Coleman, R.G., and Bird, D.K. (2004) H2-rich fluids from serpentinization: Geochemical and biotic implications. Proceedings of the National Academy of Sciences of the United States of America, 101, 12818–12823.

Speicher, E.A., Dyar, M.D., Gunter, M.E., Lanzirotti, A., Tucker, J.M., Peel, S.E., Brown, E.B., and Delaney, J.S. (2011) Synchrotron micro-XANES analysis of Fe3+ in oriented amphiboles. In 42nd Lunar and Planetary Science Conference p. Abstract #2287. Lunar and Planetary Institute, Houston.

Streit, E., Kelemen, P., and Eiler, J. (2012) Coexisting serpentine and quartz from carbonate-bearing serpentinized peridotite in the Samail Ophiolite, Oman. Contributions to Mineralogy and Petrology, 164, 821–837.

Taylor, R.M., Hansen, H.C.B., and Stanger, G. (1991) On the genesis and composition of natural pyroaurite. Clay Minerals, 26, 297–309.

Templeton, A.S., Knowles, E.J., Eldridge, D.L., Arey, B.W., Dohnalkova, A.C., Webb, S.M., Bailey, B.E., Tebo, B.M., and Staudigel, H. (2009) A seafloor microbial biome hosted within incipient ferromanganese crusts. Nature Geoscience, 2, 872–876.

Toner, B.M., Fakra, S.C., Manganini, S.J., Santelli, C.M., Marcus, M.A., Moffett, J.W., Rouxel, O., German, C.R., and Edwards, K.J. (2009) Preservation of iron(II) by carbon-rich matrices in a hydrothermal plume. Nature Geoscience, 2, 197–201.

Toner, B.M., Marcus, M., Edwards, K., Rouxel, O., and German, C. (2012) Measuring the form of iron in hydrothermal plume particles. Oceanography, 25, 209–212.

van Aken, P.A., and Liebscher, B. (2002) Quantification of ferrous/ferric ratios in minerals: New evaluation schemes of Fe L23 electron energy-loss near-edge spectra. Physics and Chemistry of Minerals, 29, 188–200.

Vidal, O., De Andrade, V., Lewin, E., Munoz, M., Parra, T., and Pascarelli, S. (2006) P–T-deformation-Fe3+/Fe2+ mapping at the thin section scale and comparison with XANES

mapping: Application to a garnet-bearing metapelite from the Sambagawa metamorphic belt (Japan). Journal of Metamorphic Geology, 24, 669–683.

Votyakov, S.L., Chashchukhin, I.S., Bykov, V.N., and Mironov, A.B. (1993) Behavior of Fe ions in minerals of ultrabasites during serpentinization. Geochemistry International, 30, 75–75.

Waychunas, G.A., Apted, M.J., and Brown, G.E. (1983) X-ray K-edge absorption spectra of Fe minerals and model compounds: Near-edge structure. Physics and Chemistry of Minerals, 10, 1–9.

Wilke, M., Farges, F., Petit, P.-E., Brown, G.E., and Martin, F. (2001) Oxidation state and coordination of Fe in minerals: An Fe K-XANES spectroscopic study. American Mineralogist, 86, 714–730.

Yan, L., Zhao, J., Toellner, T.S., Divan, R., Xu, S., Cai, Z., Boesenberg, J.S., Friedrich, J.M., Cramer, S.P., and Alp, E.E. (2012) Exploration of synchrotron Mössbauer microscopy with micrometer resolution: Forward and a new backscattering modality on natural samples. Journal of Synchrotron Radiation, 19, 814–820.

Ying, S.C., Masue-Slowey, Y., Kocar, B.D., Griffis, S.D., Webb, S., Marcus, M.A., Francis, C.A., and Fendorf, S. (2013) Distributed microbially- and chemically-mediated redox processes controlling arsenic dynamics within Mn-/Fe-oxide constructed aggregates. Geochimica et Cosmochimica Acta, 104, 29–41.

This is a preprint, the final version is subject to change, of the American Mineralogist (MSA)
Cite as Authors (Year) Title. American Mineralogist, in press.
DOI: https://doi.org/10.2138/am-2020-7359

Figure Captions

Figure 1

Schematic illustrating the steps for collecting and processing Fe K-edge XANES data to derive Fe(III)/∑Fe. (A) Fe fluorescence yield data is collected at nine discrete energies along the pre-edge peak (7108 - 7118 eV), and one additional energy above the edge (7200 eV) (blue points). A full XANES spectrum collected at the same spot in the map, is also shown for comparison (black curve). (B) After normalizing the pre-edge points to the Fe fluorescence above the edge, an exponential baseline is fit through two points such that all other points fall above the baseline. (C) The baseline is subtracted, and the points falling between the selected baseline points are integrated in order to calculate the centroid and intensity. (D) The extracted centroid and intensity values are plotted onto the calibrated Fe redox variogram, and the Fe(III)/∑Fe can be read off of the variogram tielines (errors bars represent uncertainty on the centroid and intensity due to shot noise prior to smoothing; the error on the actual Fe(III)/∑Fe is ±14%).

Figure 2

Plane-polarized light photomicrograph of OM14-07. The area selected for Raman hyperspectral mapping is outlined in blue, and corresponds to the approximate area of the Fe XRF maps.

Figure 3

Raman hyperspectral score map (A) and component spectra (B). Raman components and scores are derived from multivariate curve resolution (MCR). The intensities of some spectra

This is a preprint, the final version is subject to change, of the American Mineralogist (MSA)
Cite as Authors (Year) Title. American Mineralogist, in press.
DOI: https://doi.org/10.2138/am-2020-7359

1322 were multiplied to emphasize their peaks (x5, x20). Colors in the map (A) indicate the
1323 contribution of the spectral end-members to the fit of each pixel's Raman spectrum (B).
1324
1325 **Figure 4**
1326 Quantitative elemental maps derived from EPMA mapping, shown in elemental weight
1327 %. The mapped region is larger than and encompasses the areas of the Raman and Fe redox XRF
1328 maps. Pixels shown in white have concentrations higher than the indicated color scale, or are
1329 otherwise invalid.
1330
1331 **Figure 5**
1332 Synchrotron-based μXRF-derived images of OM14-07. Fe fluorescence excited at 7200
1333 eV (A), illustrates the qualitative variations in Fe concentration. Energy position of the centroid
1334 of the pre-edge feature after gaussian smoothing (B) which is mostly affected by variation in
1335 Fe(III)/∑Fe. Integrated intensity of the pre-edge feature after gaussian smoothing (C) which
1336 mainly illustrates variation in Fe-coordination. Raw/unsmoothed centroid and intensity maps are
1337 shown in Supplementary Information Figure 1. Abbreviations: Ol = olivine, Srp = serpentine,
1338 Pra = pyroaurite, Hdx = hydroxide phase, Mgt = magnetite.
1339
1340 **Figure 6**
1341 Fe redox variogram, showing kernel density of pixels after gaussian smoothing applied to
1342 the centroid and intensity maps. Fe(III)/∑Fe is given by the variogram tielines at 10% intervals.
1343 Contour line envelopes that encompass 50%, 75%, and 90% of the total pixel kernel density are

1344 also shown. The unsmoothed centroid and intensity values are plotted on the variogram in the
1345 Supplementary Information Figure 2.
1346
1347 **Figure 7**
1348 (A) Map of the Fe(III)/∑Fe ratio. (B) Map showing Fe(II) and Fe(III) abundance, varying
1349 from green to red as shown in the legend. This map is constructed by combining the Fe
1350 fluorescence signal (collected above the Fe K edge at 7200 eV, Figure 4A) which represents the
1351 Fe concentration with the Fe(III)/∑Fe map. Bright pixels represent areas rich in Fe(II) and/or
1352 Fe(III), while dark pixels are Fe-poor. In both (A) and (B), pixels without valid redox estimates
1353 are shown in black (to the right of the ^{VI}Fe(III)-^{IV}Fe(III) join), white (below the ^{VI}Fe(II)-
1354 ^{VI}Fe(III) join), and magenta (above the ^{VI}Fe(II)-^{IV}Fe(III) join), according to where they plot
1355 relative to the Fe redox variogram. Abbreviations: Ol = olivine, Srp = serpentine, Pra =
1356 pyroaurite, Hdx = hydroxide phase, Mgt = magnetite.
1357
1358 **Figure 8**
1359 Fe redox state of mineral phases identified by Raman spectroscopy. (A) Fe redox
1360 variogram with envelopes for major mineral phases. Envelopes are drawn to encompass 90% of
1361 the kernel density of the 500 purest pixels of each phase in terms of their Raman spectra, and are
1362 shown with transparency in order to show areas where multiple envelopes overlap. (B)
1363 Fe(III)/∑Fe kernel density plot showing the distribution of values observed for the major Fe-
1364 bearing minerals identified by Raman spectroscopy.
1365
1366 **Figure 9**

This is a preprint, the final version is subject to change, of the American Mineralogist (MSA)
Cite as Authors (Year) Title. American Mineralogist, in press.
DOI: https://doi.org/10.2138/am-2020-7359

A: Fe(III)/∑Fe determined using full-resolution XANES spectra, collected within the sample or from three Fe-bearing phyllosilicate standards with intermediate Fe(III)/∑Fe that were not used in the variogram calibration, using traditional peak-fitting approach versus the down-sampled map quantification approach. The 1:1 line ± 6.2% root mean squared error is also shown. B: Fe(III) determined from the down-sampled map quantification versus the known Fe(III)/∑Fe (from wet chemical analysis, Mössbauer spectroscopy, and EPMA) of three Fe-bearing phyllosilicate standards with intermediate Fe(III)/∑Fe that were not used in the variogram calibration. Horizontal error bars represent the analytical uncertainty reported in Bourdelle et al. (2013), while vertical error bars represent the standard deviation of three replicate spot XANES per standard.

This is a preprint, the final version is subject to change, of the American Mineralogist (MSA)
Cite as Authors (Year) Title. American Mineralogist, in press.
DOI: https://doi.org/10.2138/am-2020-7359

Table 1: Elemental compositions of mineral end-members from EPMA

wt %	Olivine	Serpentine	Magnetite	Pyroaurite	Hydroxide Phase
SiO_2	40.34	40.77	6.73	0.92	0.85
MgO	48.59	40.26	7.52	33.95	45.47
FeO_T	9.29	2.71	73.48	19.32	17.57
Al_2O_3	0.02	0.03	0.25	0.02	0.04
Cr_2O_3	0.03	0.02	0.02	0.01	0.01
NiO	0.36	0.10	0.17	0.56	0.32
CaO	0.05	0.05	0.05	0.02	0.28
Na_2O	0.02	0.03	0.05	0.01	0.01
Cl^-	0.01	0.07	0.03	0.16	0.06
S^{2-}	0.02	0.05	0.01	0.03	0.03
Total	98.73	84.09	88.31	54.99	64.63
X_{Mg}	0.90	0.96	0.15	0.76	0.82

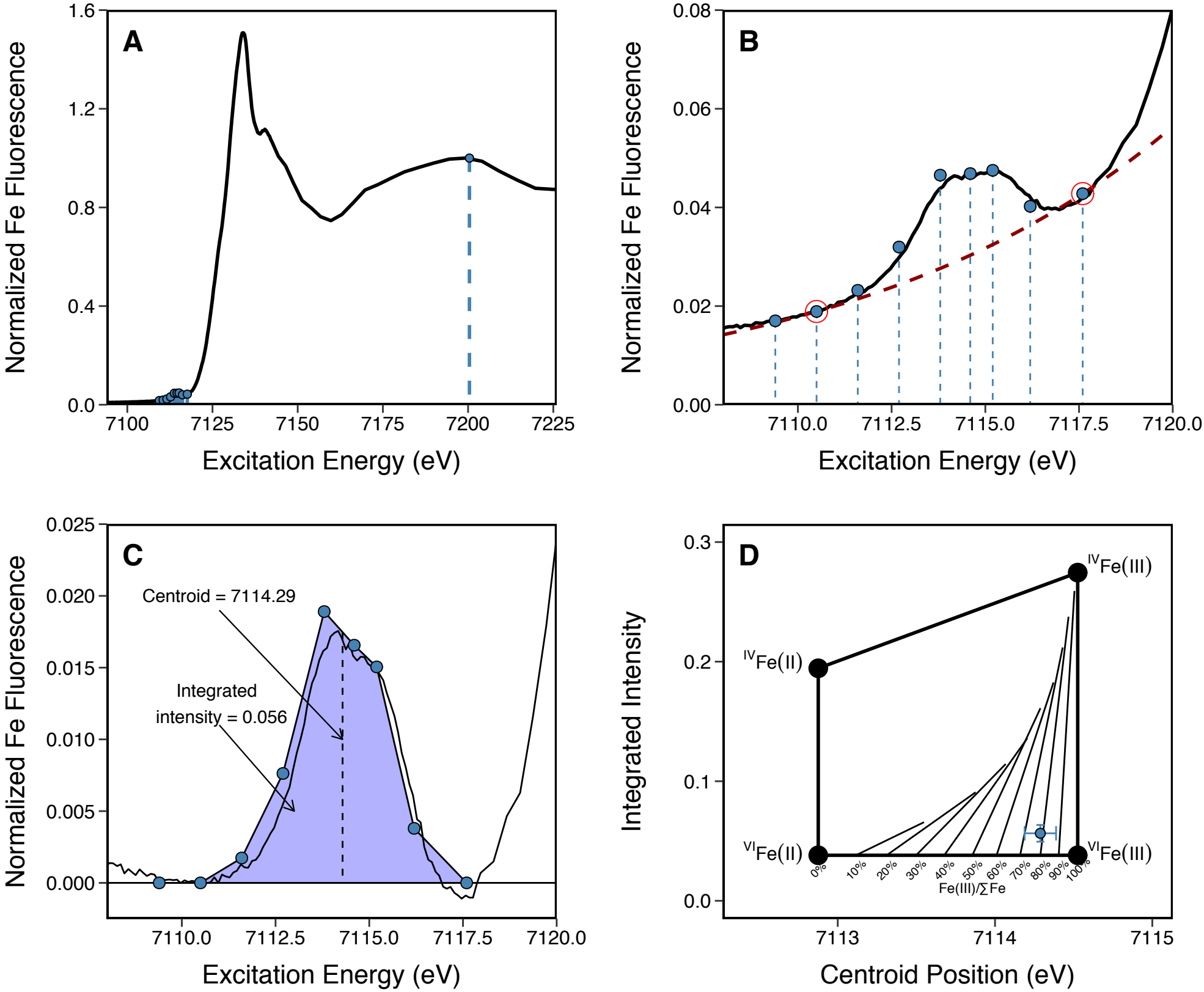
A
Normalized Fe Fluorescence
Excitation Energy (eV)
B
Normalized Fe Fluorescence
Excitation Energy (eV)
C
Centroid = 7114.29
Integrated
intensity = 0.056
Normalized Fe Fluorescence
Excitation Energy (eV)
D
IVFe(III)
IVFe(II)
VIFe(II)
VIFe(III)
0%
10%
20%
30%
40%
50%
60%
70%
80%
90%
100%
Fe(III)/∑Fe
Integrated Intensity
Centroid Position (eV)

Figure 1

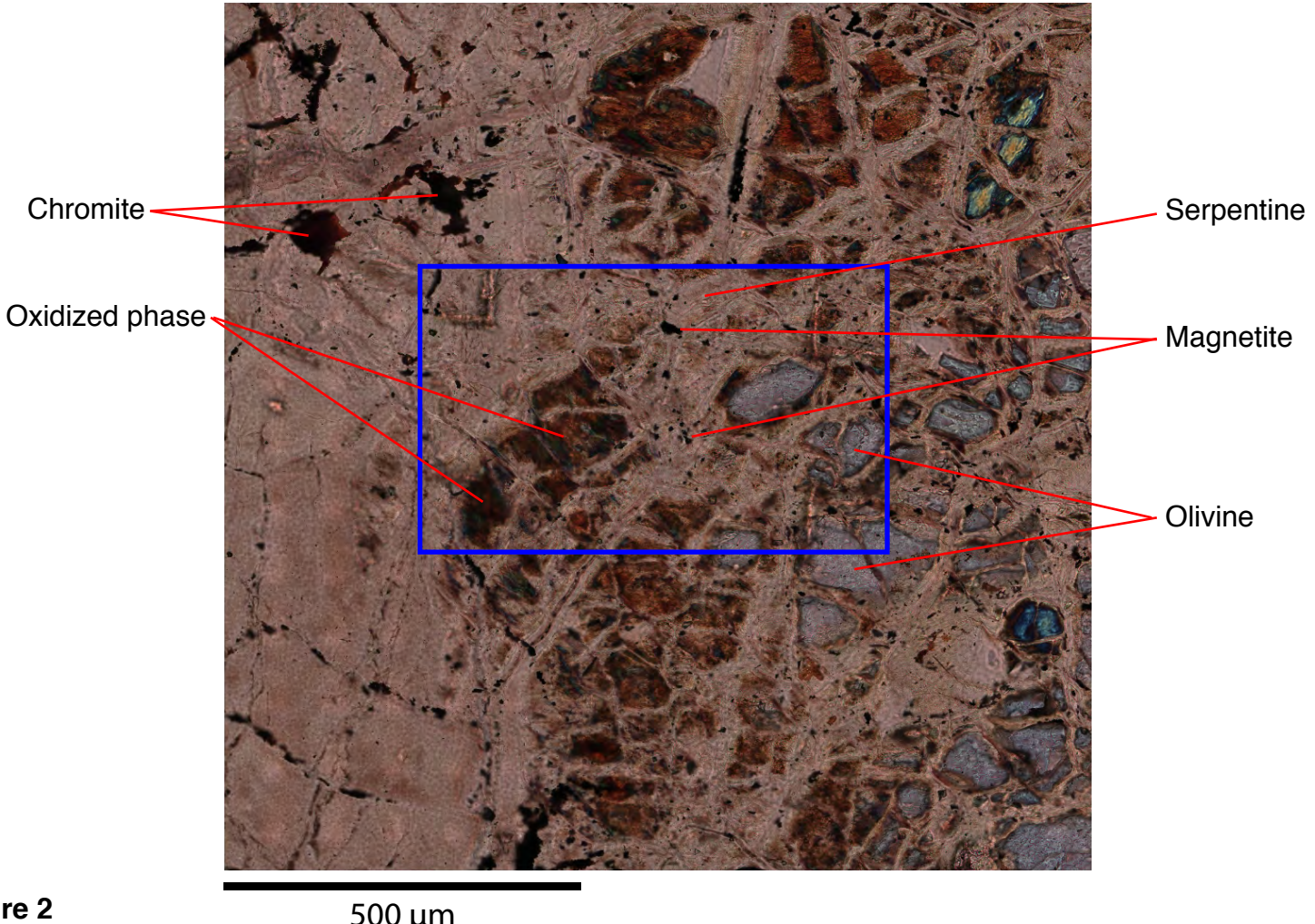
Chromite
Oxidized phase
Serpentine
Magnetite
Olivine
500 µm

Figure 2

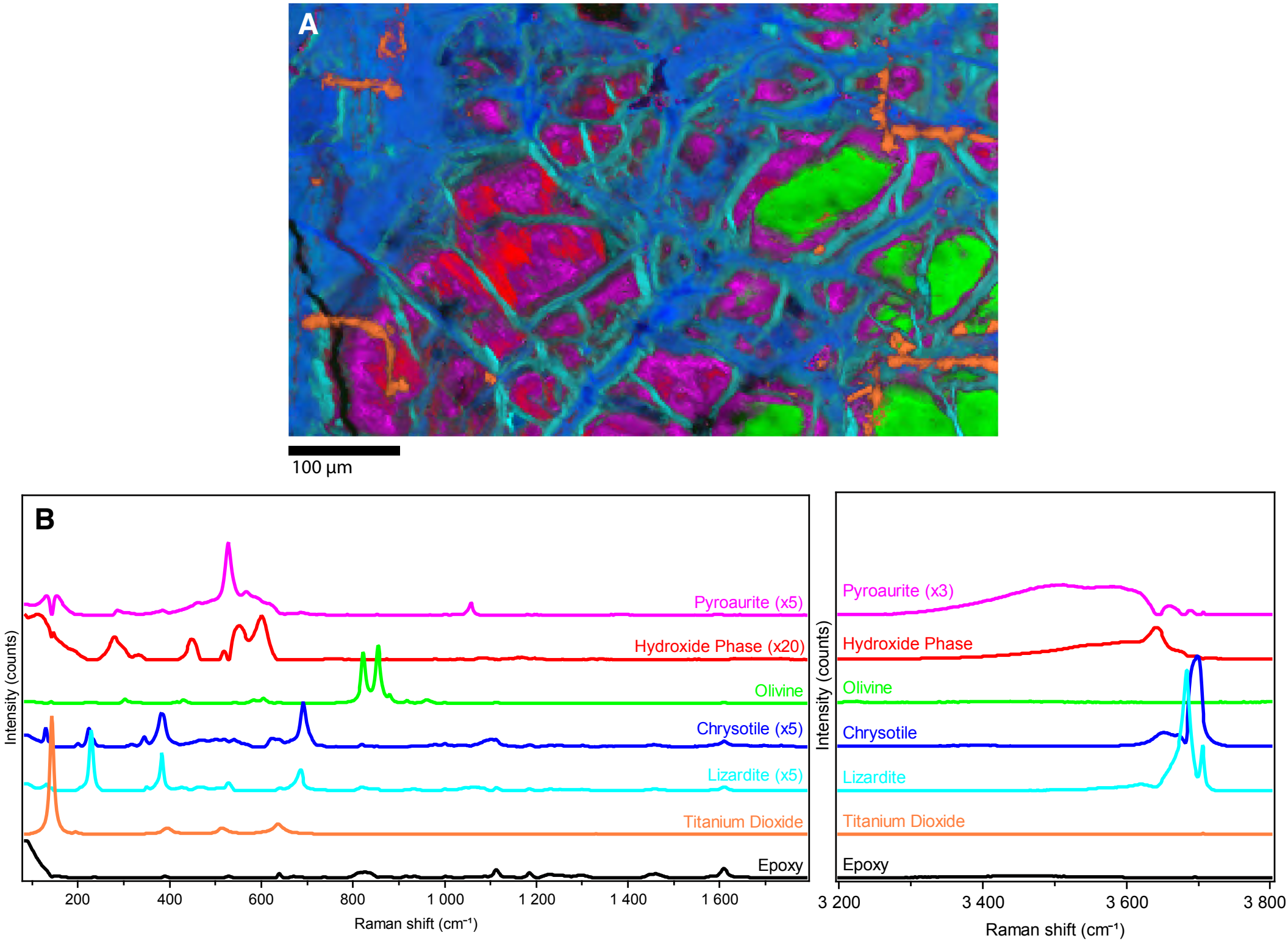
A
100 µm
B
Pyroaurite (x5)
Hydroxide Phase (x20)
Olivine
Chrysotile (x5)
Lizardite (x5)
Titanium Dioxide
Epoxy
Intensity (counts)
200
400
600
800
1 000
1 200
1 400
1 600
Raman shift (cm⁻¹)
Pyroaurite (x3)
Hydroxide Phase
Olivine
Chrysotile
Lizardite
Titanium Dioxide
Epoxy
Intensity (counts)
3 200
3 400
3 600
3 800
Raman shift (cm⁻¹)

Figure 3

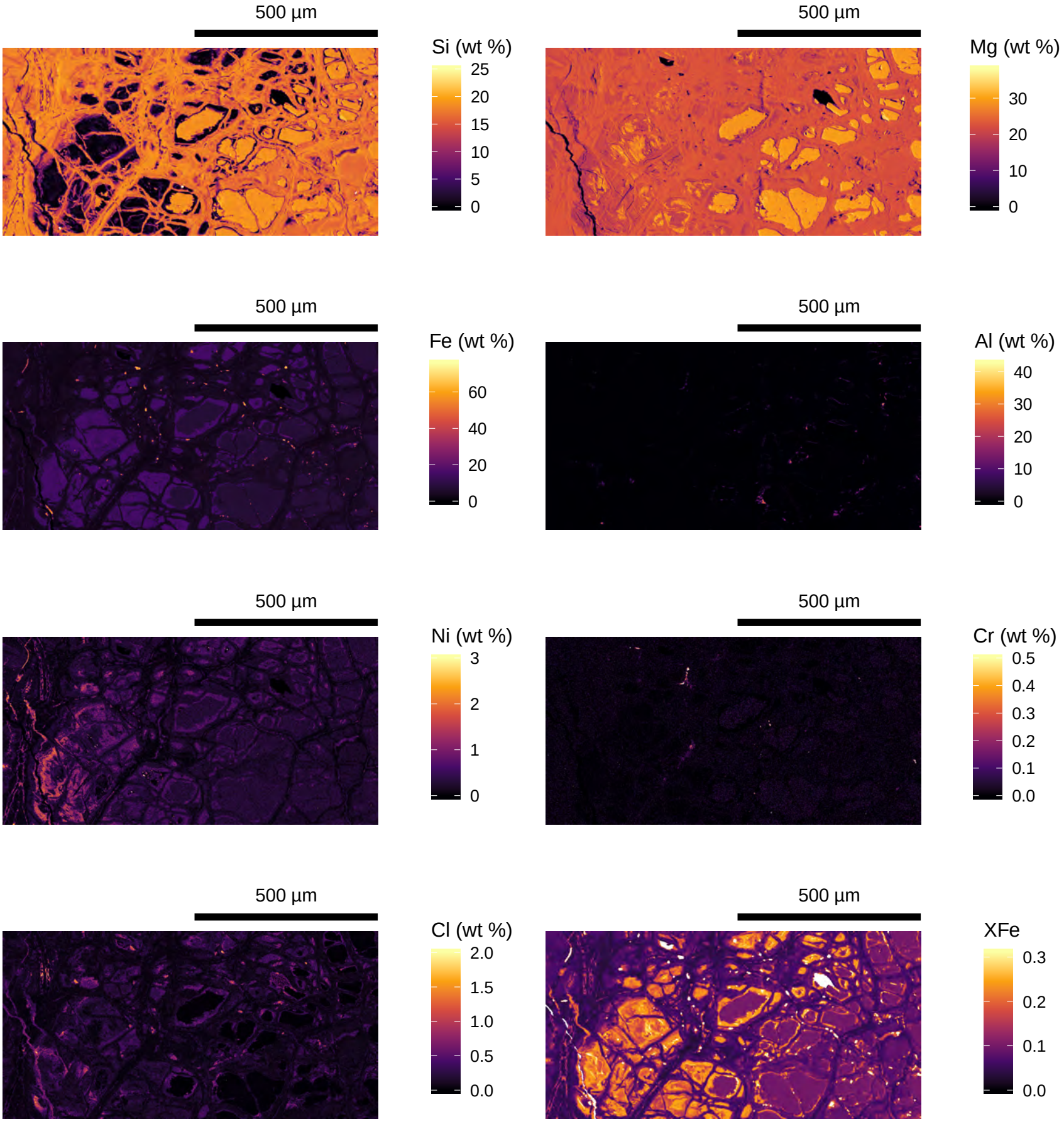
500 µm
Si (wt %)
25
20
15
10
5
0
500 µm
Mg (wt %)
30
20
10
0
500 µm
Fe (wt %)
60
40
20
0
500 µm
Al (wt %)
40
30
20
10
0
500 µm
Ni (wt %)
3
2
1
0
500 µm
Cr (wt %)
0.5
0.4
0.3
0.2
0.1
0.0
500 µm
Cl (wt %)
2.0
1.5
1.0
0.5
0.0
500 µm
XFe
0.3
0.2
0.1
0.0

Figure 4

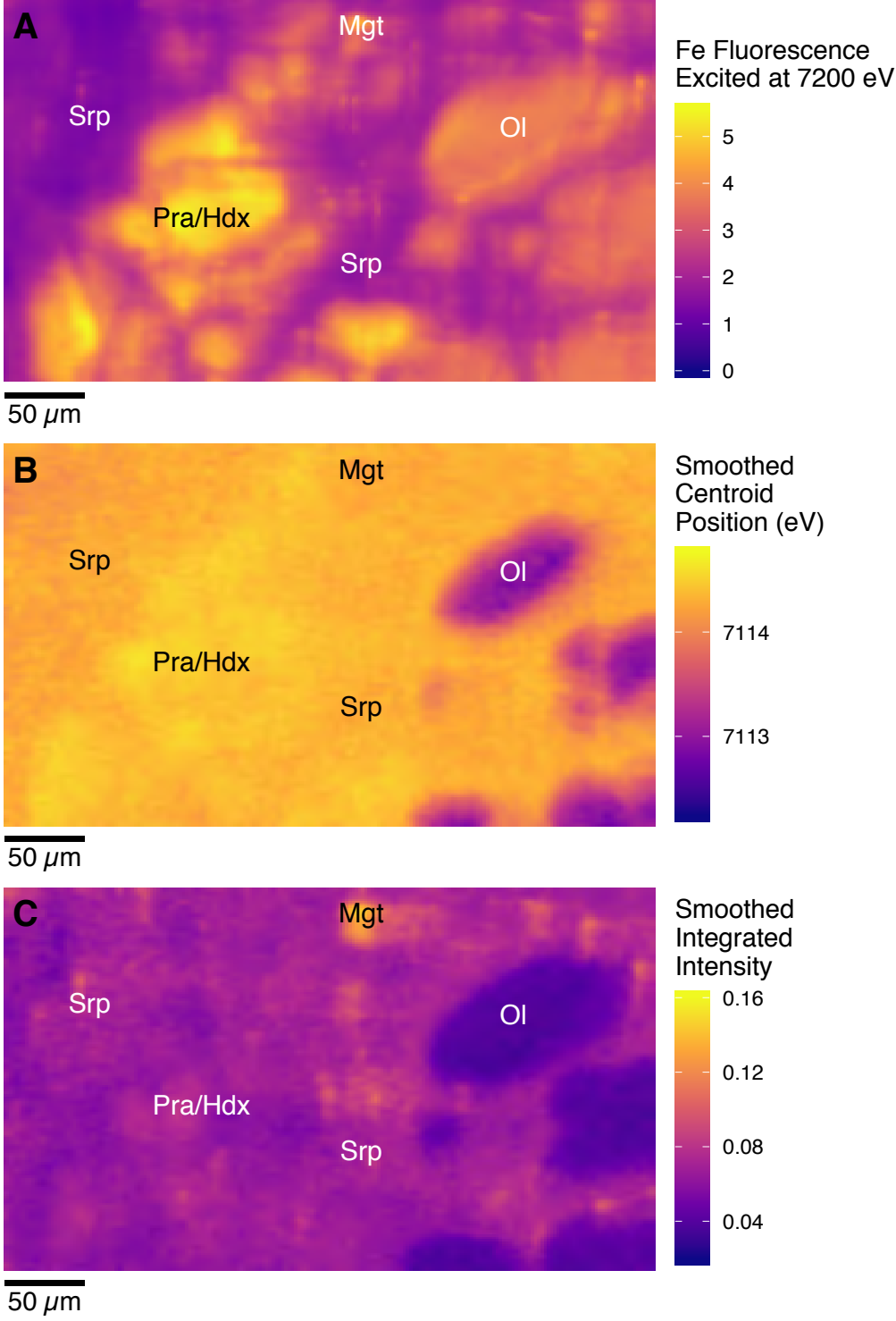
A
Mgt
Srp
Ol
Pra/Hdx
Srp
Fe Fluorescence
Excited at 7200 eV
5
4
3
2
1
0
50 μm
B
Mgt
Srp
Ol
Pra/Hdx
Srp
Smoothed
Centroid
Position (eV)
7114
7113
50 μm
C
Mgt
Srp
Ol
Pra/Hdx
Srp
Smoothed
Integrated
Intensity
0.16
0.12
0.08
0.04
50 μm

Figure 5

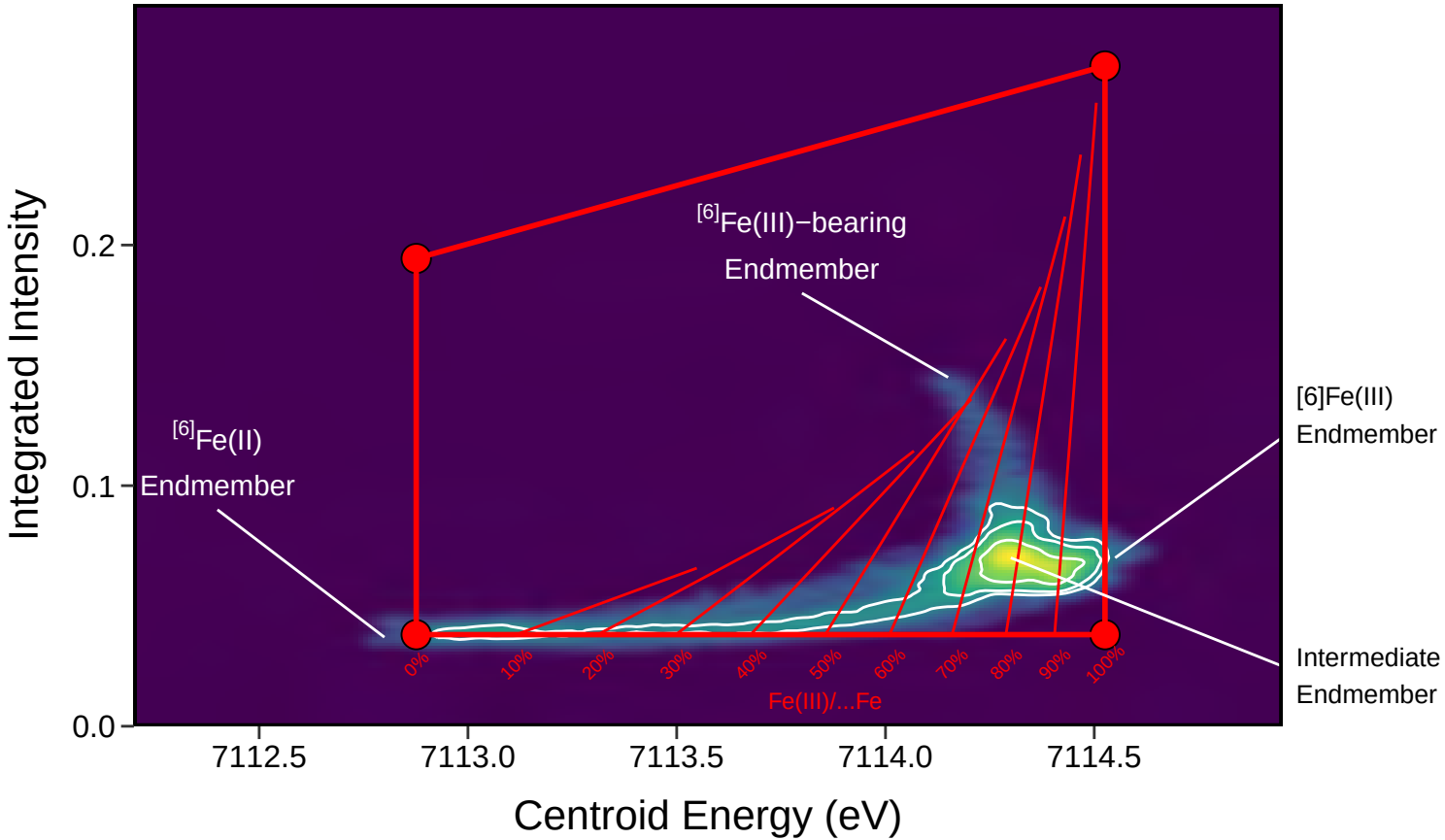
Integrated Intensity
0.2
0.1
0.0
7112.5
7113.0
7113.5
7114.0
7114.5
Centroid Energy (eV)
[6]Fe(III)−bearing
Endmember
[6]Fe(II)
Endmember
[6]Fe(III)
Endmember
Intermediate
Endmember
0%
10%
20%
30%
40%
50%
60%
70%
80%
90%
100%
Fe(III)/...Fe

Figure 6

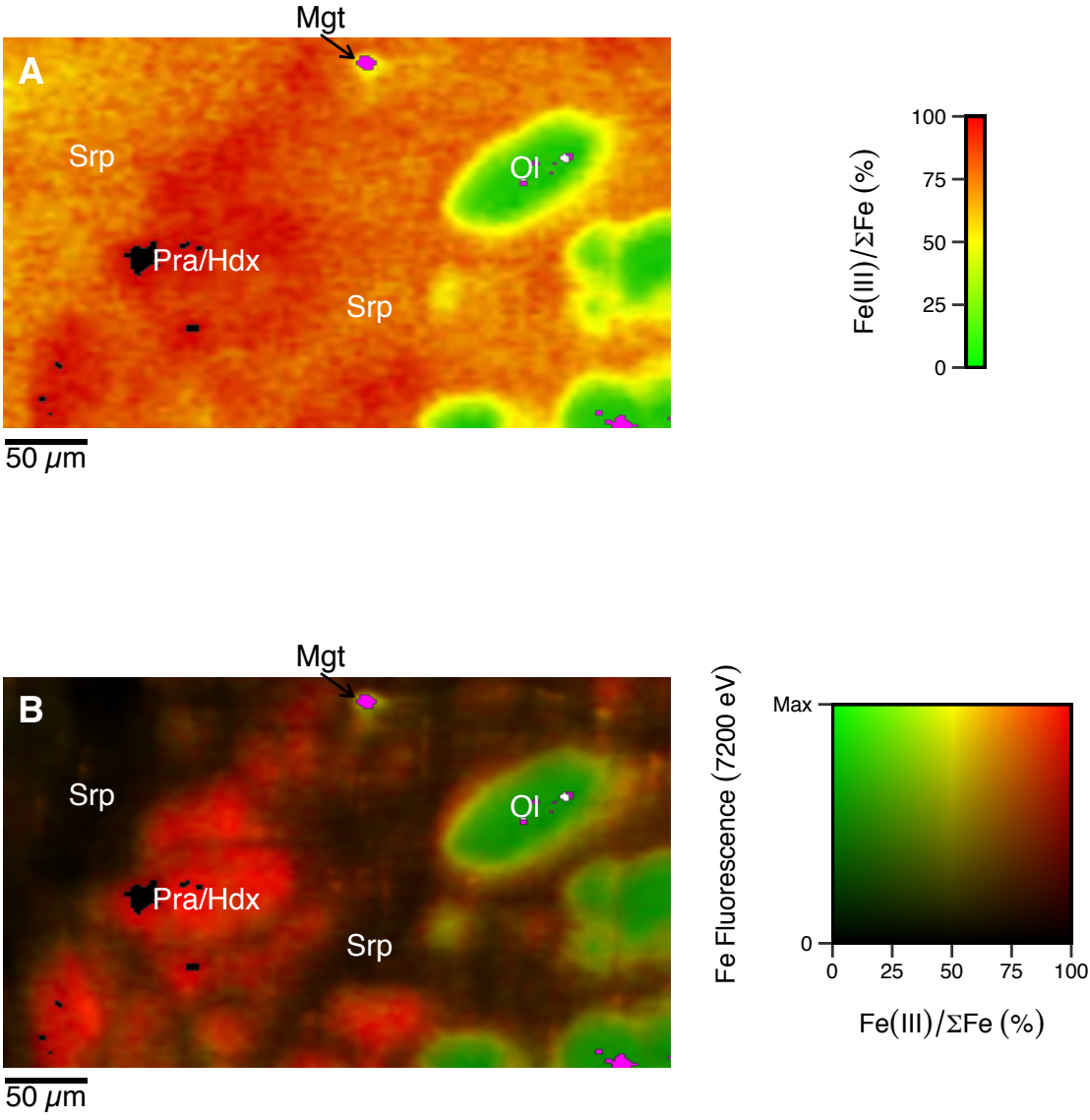
A
Mgt
Srp
Ol
Pra/Hdx
Srp
50 μm
100
75
50
25
0
Fe(III)/ΣFe (%)
B
Mgt
Srp
Ol
Pra/Hdx
Srp
50 μm
Max
0
Fe Fluorescence (7200 eV)
0
25
50
75
100
Fe(III)/ΣFe (%)

Figure 7

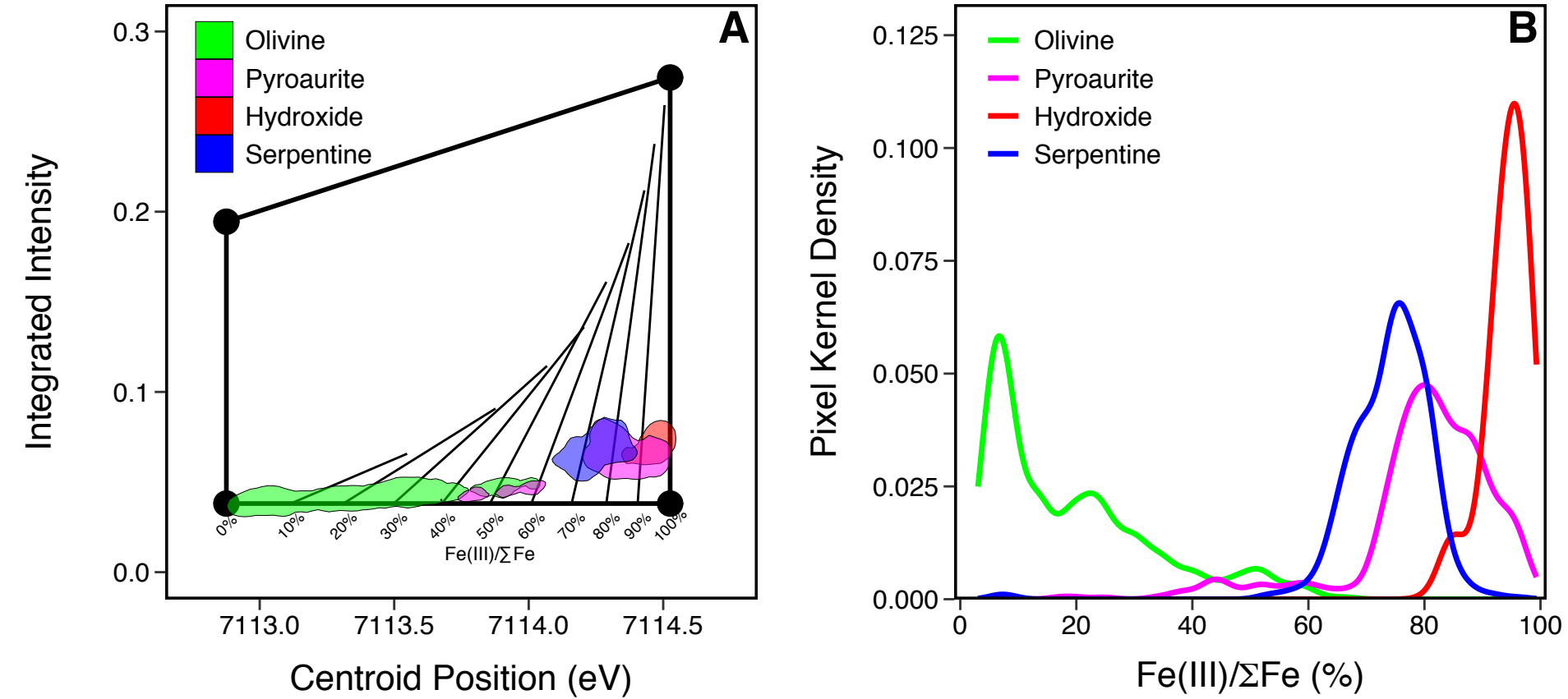
A
Olivine
Pyroaurite
Hydroxide
Serpentine
Integrated Intensity
0.3
0.2
0.1
0.0
0%
10%
20%
30%
40%
50%
60%
70%
80%
90%
100%
Fe(III)/∑Fe
7113.0
7113.5
7114.0
7114.5
Centroid Position (eV)
B
Olivine
Pyroaurite
Hydroxide
Serpentine
Pixel Kernel Density
0.125
0.100
0.075
0.050
0.025
0.000
0
20
40
60
80
100
Fe(III)/ΣFe (%)

Figure 8

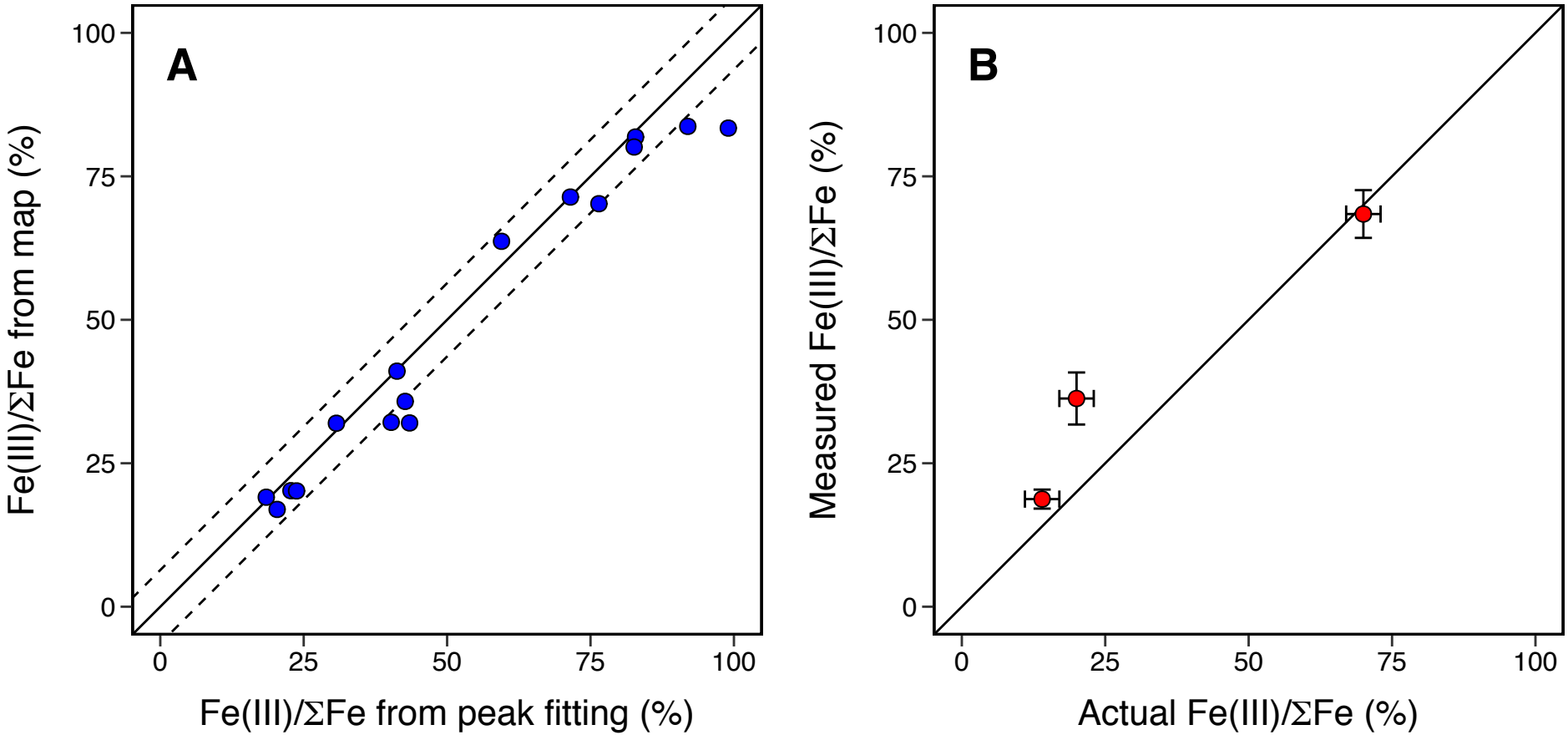
A
100
75
50
25
0
0
25
50
75
100
Fe(III)/ΣFe from map (%)
Fe(III)/ΣFe from peak fitting (%)
B
100
75
50
25
0
0
25
50
75
100
Measured Fe(III)/ΣFe (%)
Actual Fe(III)/ΣFe (%)

Figure 9